The Astrophysical Journal Letters, 969:L11 (18pp), 2024 July 1 https://doi.org/10.3847/2041-8213/ad527a

SN 2023zaw: An Ultrastripped, Nickel-poor Supernova from a Low-mass Progenitor

Kaustav K. Das[1], Christoffer Fremling[2], Mansi M. Kasliwal[1], Steve Schulze[3], Jesper Sollerman[4], Viraj Karambelkar[1], Sam Rose[1], Shreya Anand[1], Igor Andreoni[5,6,7], Marie Aubert[8], Sean J. Brennan[4], S. Bradley Cenko[5,9], Michael W. Coughlin[10], B. O'Connor[11], Kishalay De[12], Jim Fuller[1], Matthew Graham[1], Erica Hammerstein[6], Annastasia Haynie[13,14], K-Ryan Hinds[15], Io Kleiser[1], S. R. Kulkarni[1], Zeren Lin[1], Chang Liu[3,16], Ashish A. Mahabal[17,18], Christopher Martin[1], Adam A. Miller[3,16], James D. Neill[1], Daniel A. Perley[15], Priscila J. Pessi[4], Nikolaus Z. Prusinski[1], Josiah Purdum[2], Vikram Ravi[1], Ben Rusholme[1], Samantha Wu[1], Avery Wold[1], and Lin Yan[2]

[1] Cahill Center for Astrophysics, California Institute of Technology, MC 249-17, 1200 E California Boulevard, Pasadena, CA 91125, USA; kdas@astro.caltech.edu
[2] Caltech Optical Observatories, California Institute of Technology, Pasadena, CA 91125, USA
[3] Center for Interdisciplinary Exploration and Research in Astrophysics (CIERA), Northwestern University, 1800 Sherman Ave., Evanston, IL 60201, USA
[4] The Oskar Klein Centre, Department of Astronomy, Stockholm University, AlbaNova, SE-10691 Stockholm, Sweden
[5] Joint Space-Science Institute, University of Maryland, College Park, MD 20742, USA
[6] Department of Astronomy, University of Maryland, College Park, MD 20742, USA
[7] Astrophysics Science Division, NASA Goddard Space Flight Center, Mail Code 661, Greenbelt, MD 20771, USA
[8] Université Clermont-Auvergne, CNRS, LPCA, 63000 Clermont-Ferrand, France
[9] Astrophysics Science Division, NASA Goddard Space Flight Center, MC 661, Greenbelt, MD 20771, USA
[10] School of Physics and Astronomy, University of Minnesota, Minneapolis, MN 55455, USA
[11] McWilliams Center for Cosmology and Astrophysics, Department of Physics, Carnegie Mellon University, Pittsburgh, PA 15213, USA
[12] MIT-Kavli Institute for Astrophysics and Space Research 77 Massachusetts Ave. Cambridge, MA 02139, USA
[13] Department of Physics and Astronomy, University of Southern California, Los Angeles, CA 90089, USA
[14] The Observatories of the Carnegie Institution for Science, 813 Santa Barbara St., Pasadena, CA 91101, USA
[15] Astrophysics Research Institute, Liverpool John Moores University, IC2, Liverpool L3 5RF, UK
[16] Department of Physics and Astronomy, Northwestern University, 2145 Sheridan Rd., Evanston, IL 60208, USA
[17] Division of Physics, Mathematics and Astronomy, California Institute of Technology, Pasadena, CA 91125, USA
[18] Center for Data Driven Discovery, California Institute of Technology, Pasadena, CA 91125, USA
Received 2024 March 14; revised 2024 May 16; accepted 2024 May 24; published 2024 June 25

Abstract

We present SN 2023zaw—a subluminous ($M_r = -16.7$ mag) and rapidly evolving supernova ($t_{1/2,r} = 4.9$ days), with the lowest nickel mass ($\approx 0.002\,M_\odot$) measured among all stripped-envelope supernovae discovered to date. The photospheric spectra are dominated by broad He I and Ca near-infrared emission lines with velocities of $\sim 10{,}000-12{,}000$ km s^{-1}. The late-time spectra show prominent narrow He I emission lines at ~ 1000 km s^{-1}, indicative of interaction with He-rich circumstellar material. SN 2023zaw is located in the spiral arm of a star-forming galaxy. We perform radiation-hydrodynamical and analytical modeling of the lightcurve by fitting with a combination of shock-cooling emission and nickel decay. The progenitor has a best-fit envelope mass of $\approx 0.2\,M_\odot$ and an envelope radius of $\approx 50\,R_\odot$. The extremely low nickel mass and low ejecta mass ($\approx 0.5\,M_\odot$) suggest an ultrastripped SN, which originates from a mass-losing low-mass He-star (zero-age main-sequence mass $< 10\,M_\odot$) in a close binary system. This is a channel to form double neutron star systems, whose merger is detectable with LIGO. SN 2023zaw underscores the existence of a previously undiscovered population of extremely low nickel mass ($<0.005\,M_\odot$) stripped-envelope supernovae, which can be explored with deep and high-cadence transient surveys.

Unified Astronomy Thesaurus concepts: Core-collapse supernovae (304); Type Ib supernovae (1729); Compact binary stars (283); Stellar mass loss (1613); Roche lobe overflow (2155)

Materials only available in the online version of record: machine-readable tables

1. Introduction

Modern wide-field and high-cadence transient surveys such as the Zwicky Transient Facility (ZTF; Bellm et al. 2019; Graham et al. 2019) and the Asteroid Terrestrial-impact Last Alert System (ATLAS; Tonry et al. 2018; Smith et al. 2020) have expanded the discovery space of unusual supernovae (SNe). The class of rapidly evolving, faint SNe constitutes such a population of peculiar SNe that evolve on the shortest timescales of a few days and have a peak absolute magnitude fainter than −17 mag. There are only a handful of well-studied examples in the literature—SN 2005ek (Drout et al. 2013), SN 2010X (Kasliwal et al. 2010), iPTF14gqr (De et al. 2018a), SN 2018kzr (McBrien et al. 2019), SN 2019dge (Yao et al. 2020), SN 2019wxt (Agudo et al. 2023; Shivkumar et al. 2023), SN 2019bkc (Chen et al. 2020; Prentice et al. 2020), and SN 2022agco (Yan et al. 2023).

Despite advances in understanding the photometric and spectroscopic diversity, the class of rapidly-evolving, faint SNe progenitors and powering mechanisms remain unknown. The various theoretical scenarios include ultrastripped core-collapse SNe of massive stars that lead to binary neutron star (NS) systems (Tauris et al. 2013, 2015), nonterminal thermonuclear detonations of a helium shell on the surface of a white dwarf

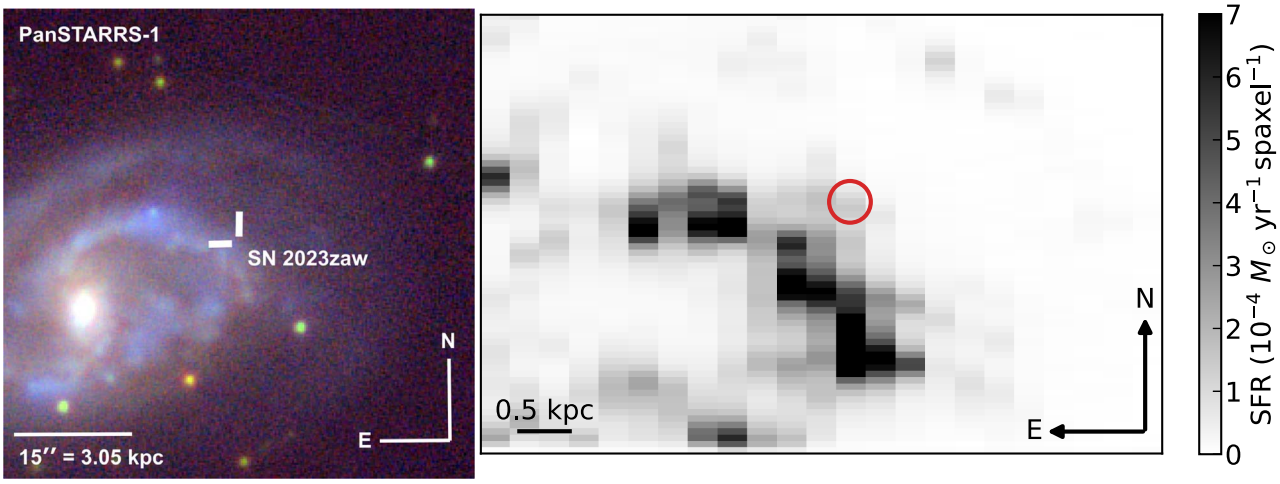

Figure 1. Left: Pan-STARRS image of the host galaxy of SN 2023zaw, UGC 03048 in the *grizy* filters. The location of the transient is indicated by the white cross at the center. Right*:* SFR map of the environment around SN 2023zaw (see Section 3.7). SN 2023zaw (position marked by the red circle) exploded in a star-forming region of the host galaxy close to regions of more vigorously star-forming regions. The image has a size of 4.1 × 6.7 kpc. The SFR scale is not corrected for attenuation.

(WD) called a ".Ia" SN (Bildsten et al. 2007; Shen et al. 2010), shock-cooling of H-poor stars with an extended envelope (Kleiser & Kasen 2014; Kleiser et al. 2018), fallback in a core-collapse SN (Zhang et al. 2008; Moriya et al. 2010), accretion-induced collapse (AIC) of a WD (Dessart et al. 2007), electron-capture SN (ECSN; Moriya & Eldridge 2016), and NS–WD mergers (Margalit & Metzger 2016).

In this Letter, we present SN 2023zaw—a Type Ib SN with the lowest nickel mass measured among all stripped-envelope SNe discovered to date. The late-time spectra are dominated by narrow He I emission lines, suggestive of interaction with He-rich circumstellar material (CSM). SN 2023zaw exhibits the most rapid rise and fade time among all stripped-envelope SNe in the literature. Additionally, it is the nearest SN among all fast and faint SNe in the literature. The photometric and spectroscopic properties suggest that it is an ultrastripped SN, originating from a progenitor with an initial mass $<10\,M_\odot$, which likely formed an NS.

2. Discovery and Follow-up Observations

2.1. Discovery

SN 2023zaw (ZTF23absbqun) was discovered with the ZTF camera (Dekany et al. 2020), which is mounted on the 48 inch Samuel Oschin Telescope at the Palomar Observatory. It was first detected at $\alpha = 04^{\rm h}29^{\rm m}20\overset{\rm s}{.}235$, $\delta = +70°25'37\overset{''}{.}52$ (J2000) on 2023 December 7, at 05:34:06 UTC and reported to the Transient Name Server[19] (Sollerman 2023). At the time of discovery, the AB apparent magnitude in the g band was 19.34 ± 0.15 mag. The transient stood out due to its faintness and extremely fast evolution (see Figure A1). It was also flagged as a fast transient candidate by the ZTFReST framework for kilonova and fast-transient discovery (Andreoni et al. 2021) and was saved as part of the magnitude-limited (Bright Transient Survey; Fremling et al. 2020) and volume-limited (Census of the Local Universe; De et al. 2020) surveys of ZTF.

SN 2023zaw is located in the UGC 03048 galaxy at a redshift of $z = 0.0101$ (Springob et al. 2005). It is located on the edge of one of its spiral arms (see Figure 1). The angular separation from the nucleus of the galaxy is $21\overset{''}{.}44$, which corresponds to a physical separation of 4.36 kpc. We correct for the Virgo, Great Attractor, and Shapley supercluster infall (Mould et al. 2000) based on the NASA Extragalactic Database[20] object page for UGC 03048. We adopt a Hubble-flow distance of 43.9 ± 3.1 Mpc, which corresponds to a distance modulus of 33.21 ± 0.15 mag.

2.2. Optical Photometry

We obtained multiple epochs of g-, r-, and i-band photometry with the ZTF camera. The images were reduced using the ZTF image analysis pipeline (Masci et al. 2019). We also perform forced photometry at the location of the transient for the ZTF images in the *gri* bands. We obtained c- and o-band photometry from the forced-photometry service of the ATLAS (Tonry et al. 2018; Smith et al. 2020; Shingles et al. 2021). We took regular cadence multiband photometry in the g, r, i, and z bands with the optical imager (IO:O) at the 2.0 m robotic Liverpool Telescope (LT; Steele et al. 2004). In addition, photometric data were obtained with the rainbow camera on the automated Palomar 60 inch telescope (P60; Cenko et al. 2006). LT and P60 images were processed using the FPipe (Fremling et al. 2016) image-subtraction pipeline with PanSTARRS (Chambers et al. 2016) reference images. The Alhambra Faint Object Spectrograph and Camera (ALFOSC) at the 2.5 m Nordic Optical Telescope was used to obtain g-, r-, and i-band photometry. The ALFOSC data was reduced using the PyNOT[21] pipeline. The collage of all the multiband lightcurves is shown in Figure 2. The photometry data are listed in Table C1.

2.3. Optical Spectroscopy

We acquired four epochs of spectroscopy with the Spectral Energy Distribution Machine (SEDM; Blagorodnova et al. 2018) on the P60. The SEDM data was reduced using the pipeline described in Rigault et al. (2019) and Kim et al. (2022).

[19] https://www.wis-tns.org/

[20] https://ned.ipac.caltech.edu/

[21] https://github.com/jkrogager/PyNOT

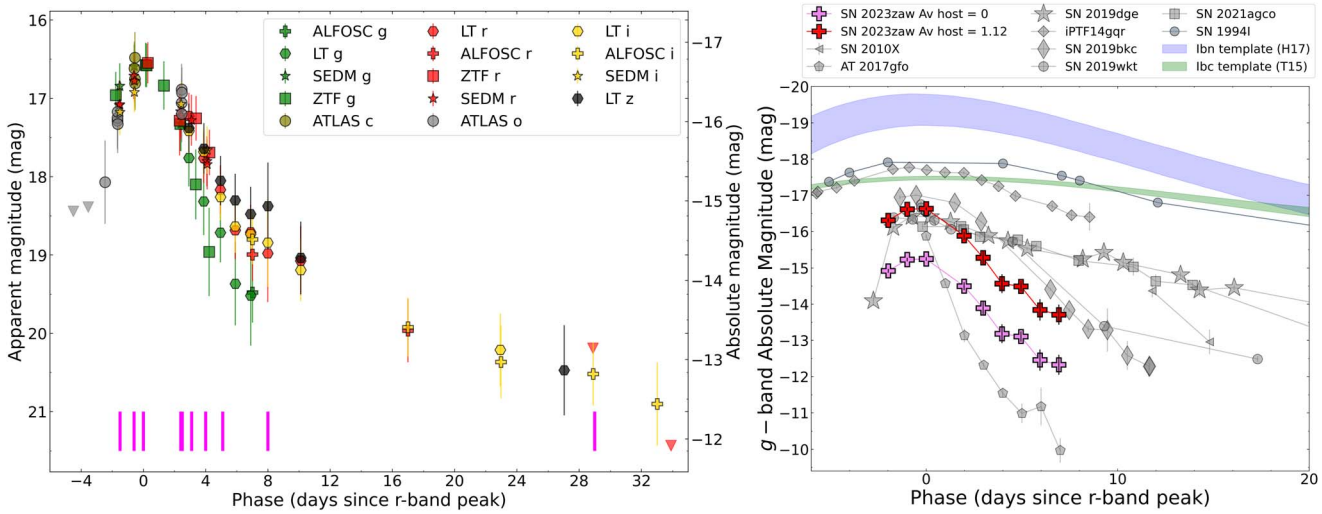

Figure 2. Left: the multiband lightcurve collage of SN 2023zaw. The x-axis shows rest-frame days since the r-band peak (MJD = 60287.7). The photometry data have been corrected for Milky Way ($A_{V,MW} = 0.77$ mag) and host extinction ($A_{V,host} = 1.12$ mag) as described in Section 3.1. The vertical magenta lines represent epochs of spectral observations. Right: the g-band lightcurve of SN 2023zaw compared with other fast-evolving transients in the literature—fast-declining Type I SNe, such as SN 2010X (Kasliwal et al. 2010); SN 2019bkc (Chen et al. 2020; Prentice et al. 2020); the kilonova AT 2017gfo (Abbott et al. 2017); and ultrastripped SN candidates—SN 2019dge (Yao et al. 2020), iPTF14gqr (De et al. 2018b), SN 2019wxt (Agudo et al. 2023; Shivkumar et al. 2023), and SN 2022agco (Yan et al. 2023). We also compare with Type Ibc and Type Ibn SN lightcurve templates from Taddia et al. (2015) and Hosseinzadeh et al. (2017), respectively.

We obtained three epochs of spectroscopy with the Low Resolution Imaging Spectrometer (LRIS; Oke et al. 1995) on the Keck I telescope, with data reduced using the automated LPIPE (Perley 2019) pipeline. The ALFOSC instrument at the 2.5 m Nordic Optical Telescope was used to obtain one epoch of low-resolution spectrum, which was reduced using the PyNOT[22] pipeline. We took one spectrum with the Binospec spectrograph (Fabricant et al. 2019) on the Multiple Mirror Telescope, which was reduced using the `PypeIt` package (Prochaska et al. 2020a, 2020b). We used the Keck Cosmic Web Imager (KCWI; Martin et al. 2010; Morrissey et al. 2018) to obtain spectra of the transient and its host environment. This was reduced using the KCWI data reduction pipeline.[23] We also show one spectrum observed with the Gemini-GMOS instrument from the Transient Name Server.[24] The collage of all the spectra is shown in Figure D1, and the spectroscopy log can be found in Table E1.

3. Methods and Analysis

3.1. Extinction Correction

We correct for Milky Way extinction using the dust maps from Schlafly & Finkbeiner (2011). Along the line of sight of SN 2023zaw, $E(B-V) = 0.25$ mag. For reddening corrections, we use the extinction law in Cardelli et al. (1989) with $R_V = 3.1$.

For host-extinction correction, we use the Na I D absorption lines of the host galaxy (Poznanski et al. 2012; Stritzinger et al. 2018). We measure an equivalent width of 1.5 ± 0.2 Å from the KCWI spectrum obtained at a phase of +2.5 days past r-band peak. To compute A_V, we use $A_V^{\rm host}[\rm mag] = 0.78(\pm 0.15) \times \rm EW_{NaID}[Å]$ (Stritzinger et al. 2018). We note that there are caveats in using the Na I D EW measurement to estimate host extinction, especially for low-resolution spectra (Poznanski et al. 2011) and in the presence of CSM (Phillips et al. 2013).

We plot the $g-r$ and $r-i$ colors of SN 2023zaw before and after host-extinction correction in Figure F1 and compare with other rapidly evolving transients and the Type Ib SN color template from Stritzinger et al. (2018).

3.2. Explosion Epoch Estimation

We fit for the r-band maximum epoch with a polynomial fit to the r-band photometry and obtain a peak magnitude of −16.7 mag and peak MJD of 60287.7. All phases mentioned in the Letter will be in rest-frame days measured from this r-band peak epoch. The last nondetection before the first detection was on 60283 MJD (−4.7 days), with an upper limit of −14.8 mag in the o band. We perform a power-law fit to the r-band data prior to the maximum epoch to estimate the explosion epoch. We find that the explosion epoch is 60284.4 ± 0.5 MJD (-3.3 ± 0.5 days).

3.3. Lightcurve Properties

In Figures 2 and G1, we compare the g- and r-band evolution of SN 2023zaw to other fast-evolving and subluminous transients in the literature: fast-declining Type I SNe—SN 2005ek (Drout et al. 2013), SN 2010X (Kasliwal et al. 2010), SN 2018kzr (McBrien et al. 2019), SN 2019bkc (Chen et al. 2020; Prentice et al. 2020), and the kilonova AT 2017gfo (Abbott et al. 2017) and ultrastripped SN candidates—SN 2019dge (Yao et al. 2020), iPTF14gqr (De et al. 2018b), SN 2019wxt (Agudo et al. 2023; Shivkumar et al. 2023), and SN 2022agco (Yan et al. 2023). We also compare with lightcurve templates for Type Ibn (Hosseinzadeh et al. 2017) and Type Ibc SNe (Taddia et al. 2015). SN 2023zaw is much fainter and faster evolving than the typical Type Ibn or Ibc SN. However, we note that some Type Ibn/Icn SNe also show rapid evolution: LSQ13ccw (Hosseinzadeh et al. 2017) and SN 2023emq (Pursiainen et al. 2023). We fit a polynomial to the lightcurves and measure the rise time and fade time as the

[22] https://github.com/jkrogager/PyNOT
[23] https://kcwi-drp.readthedocs.io
[24] https://www.wis-tns.org/

duration above the half maximum of the peak. SN 2023zaw has a rise time ($t_{\rm rise}^{1/2}$) of 1.8 days and a decline time ($t_{\rm dec}^{1/2}$) of 3.1 days. The time above half maximum of the peak is shorter than for all other fast-evolving faint transients in the literature (see Figures 2, A1, and G1). The lightcurve declines by 2.7 mag in 10 days in the *r* band and by 2.7 mag in 6 days in the *g* band. SN 2023zaw is only slower than kilonova AT 2017gfo and has a comparable decline timescale to SN 2019bkc and SN 2018kzr. In the *r* band, SN 2023zaw has a very sharp initial decline of $\sim$0.28 mag day^{-1} followed by a transition to a relatively slower decline rate of $\sim$0.07 mag day^{-1} after $\sim$10 days since peak. In the *g* band, SN 2023zaw shows a very sharp initial decline of $\sim$0.44 mag day^{-1} until 10 days postpeak. The peak absolute magnitude in the *r* band before and after host-extinction correction is -15.6 mag and -16.7 mag, respectively. In the *g* band, the peak absolute magnitude before and after host-extinction correction is -15.2 mag and -16.6 mag, respectively. We compare the time above half maximum and the absolute luminosity of SN 2023zaw to a sample of stripped-envelope supernovae (SESNe) detected by ZTF and other fast and faint SNe in the literature in Figure A1. SN 2023zaw shows the fastest evolution among all transients at similar luminosities.

3.4. Spectral Properties

In the early SEDM spectra taken before *r*-band peak, we see a blue, featureless continuum. We see multiple broad helium lines—He I $\lambda\lambda$5876, 6678, and 7065, in the subsequent spectra. The expansion velocity measured from the absorption in the P-Cygni profile of the He I lines evolved from 12,000 to 9700 km s^{-1} from 0 to 8 days postpeak. These He I absorption lines resemble those seen in Type Ib SNe and we obtain a decent fit to Type Ib SNe at similar or later phases using the `SuperNova Identification` (Blondin & Tonry 2007) code. This is consistent with the initial classification made by Gillanders et al. (2023). There is also a redshifted component to the He I λ5876 line profile in the spectrum taken at +8 and +29 days, probably due to asymmetrical ejecta. He I line velocities drop to $\sim$3000 km s^{-1} at a phase of 29 days. Prominent narrow He I emission lines can be seen in the LRIS spectra obtained at 29 and 61 days after peak. The FWHM velocities of the He I emission lines in the latest LRIS spectrum are $\sim 1050 \pm 100$ km s^{-1}.

In the photospheric phase, we do not see any broad O I λ7774 emission line, which is common in stripped-envelope SNe. We also see broad, high-velocity lines of the Ca II NIR triplet at $\sim$12,000 km s^{-1} as early as 2 days after peak. Such high-velocity early Ca NIR absorption lines are not seen in other fast-evolving SNe (see Figure 3). Also, unlike other rapid-declining SNe, SN 2023zaw does not reach nebular phase even at 29 days after peak. Broad nebular lines such as [O I] $\lambda\lambda$ 6300, 6364, and Ca II NIR triplet are also not seen in the latest LRIS spectrum taken at +61 days.

3.5. Bolometric Lightcurve

We bin the data in intervals of 1 day and fit with the Planck blackbody function where there are detections in at least three filters. We perform the fit using the Python EMCEE package (Foreman-Mackey et al. 2013). The blackbody temperature, radius, and luminosity thus obtained are shown in Table H1. The errors in the model parameters are determined by extracting the 16th and 84th percentiles of the posterior probability distribution. For the later epochs, where we have photometry in only one band, we use the extrapolated blackbody temperatures obtained by fitting an exponential decay function to the temperature data from previous epochs. The temperature stays roughly constant at $\approx$4000 K. For these later epochs, we also estimate the bolometric luminosity as νL_ν. These estimates agree with each other within 3σ, with the latter method slightly underestimating the bolometric luminosity as expected.

We plot the best-fit blackbody parameters and compare these with other ultrastripped SN candidates in Figure 4. We can see that the bolometric lightcurve of SN 2023zaw is similar in peak brightness to the other SNe but has a faster decline rate within the first 10 days after *r*-band peak. The decline of the bolometric luminosity slows down after around 6 days postpeak. The photospheric radius increases up to 4 days post-peak, reaching a maximum of $\sim$10,000 $R_\odot$. The temperature decreases over time, from a maximum of $\sim$17,000 K on day 0 to $\sim$4000 K on day 8.

3.6. Modeling the Lightcurve

3.6.1. Radiation-hydrodynamics Modeling

We use the pre-SN model grid presented in Wu & Fuller (2022). This grid was produced through binary evolution of He stars with an initial mass of 2.5–3 $M_\odot$ evolved up to silicon burning using the Modules for Experiments in Stellar Astrophysics code (MESA; Paxton et al. 2010). The binary systems evolved in Wu & Fuller (2022) include orbital periods of 1, 10, and 100 days. Predictions of the properties of the unbound CSM in the vicinity of each pre-SN model were also produced. In this work, we compare our data to both models with and without unbound CSM.

We use the SuperNova Explosion Code (SNEC; Morozova et al. 2015) to explode the grid of pre-SN stellar models described above. First, we exploded all models in the grid using a thermal bomb with $E_{\rm kin} = 0.4 \times 10^{51}$ erg and $M_{\rm Ni} = 0.0035\ M_\odot$, with ^{56}Ni mixed all the way through the remaining star after mass excision of 1.4 $M_\odot$ in the center.

The resulting bolometric lightcurves and expansion velocities were then compared to our data on SN 2023zaw. We find that the model Wu & Fuller (2022) produced from a He star with an initial mass of 2.651 $M_\odot$ and an orbit period of 100 days reproduces the overall behavior seen in our data well, including the expansion velocities. Other models fail to reproduce both the early cooling phase of the bolometric lightcurve (governed by the radius and mass in the bound envelope) or the late-time decline rate (governed by the total ejecta mass). To produce our best-fitting MESA+SNEC model shown in Figure 4, we modified the bound envelope radius of the raw MESA model so that it extends to $\approx$50 $R_\odot$ by cutting the model grid appropriately (compared to $\approx$110 $R_\odot$ in the raw model). This would correspond to an orbital period between 10 and 100 days. We also modified the mass excision in the center to be 1.3 $M_\odot$. These modifications result in the explosion parameters $E_{\rm kin} = 0.4 \times 10^{51}$ erg, $M_{\rm Ni} = 0.0035\ M_\odot$, with complete mixing of ^{56}Ni through the ejecta, which has a total mass of $M_{\rm ej} = 0.56\ M_\odot$, including the bound envelope. Models including the unbound CSM predicted by Wu & Fuller (2022) are largely inconsistent with our data. The luminosity during the first week can be similar to what we observe if the explosion energy is adjusted to be low ($<0.1 \times 10^{51}$ erg).

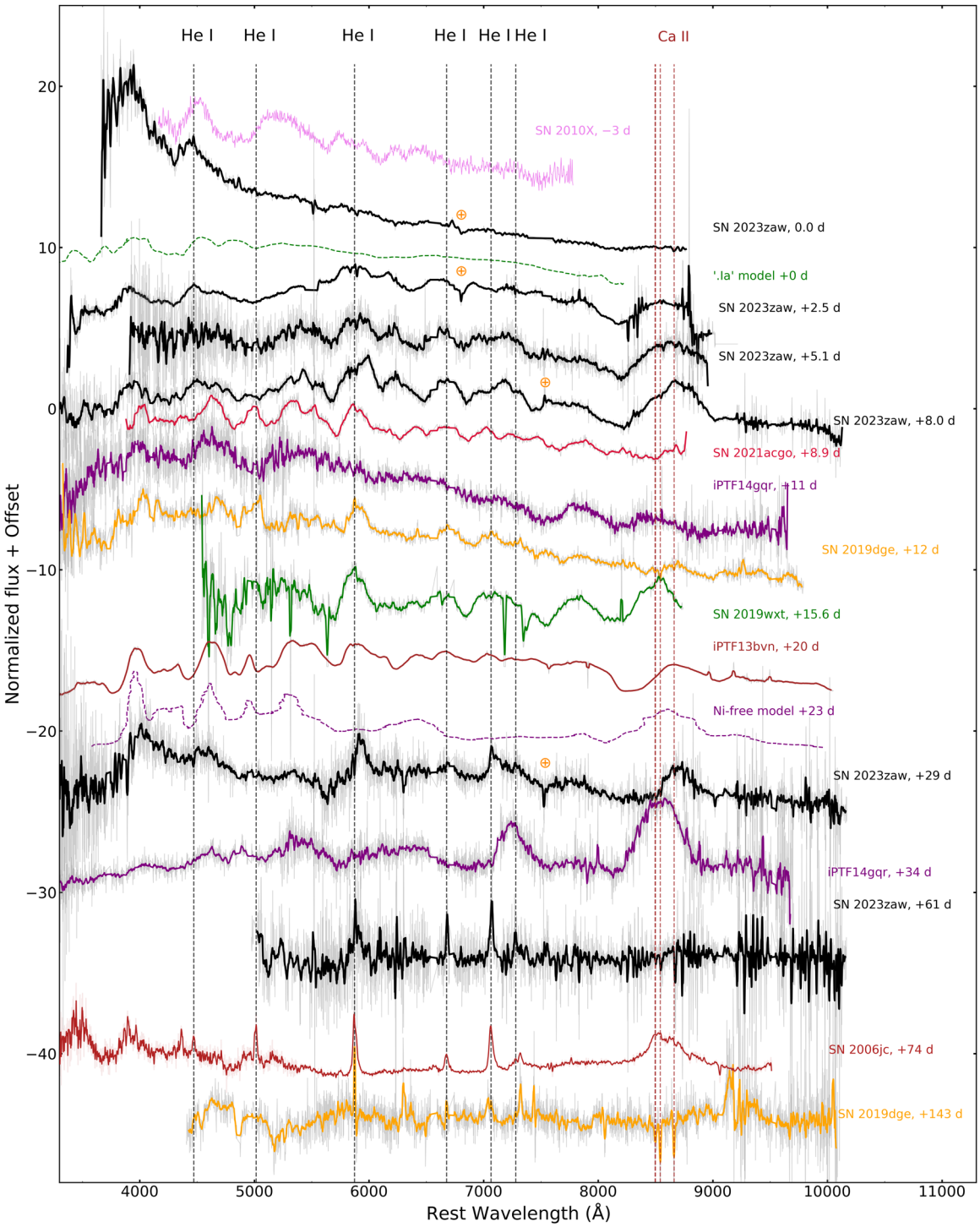

Figure 3. The spectra of SN 2023zaw (in black) compared with other fast-evolving transients in the literature: fast-declining Type I SNe—SN 2010X (Kasliwal et al. 2010); ultrastripped SNe candidates—SN 2019dge (Yao et al. 2020), iPTF14gqr (De et al. 2018b), SN 2019wxt (Agudo et al. 2023; Shivkumar et al. 2023), and SN 2022agco (Yan et al. 2023); canonical Type Ib SN—iPTF14bvn (Fremling et al. 2018); and Type Ibn—SN 2006jc (Foley et al. 2007). We also compare with theoretical predictions for ".Ia" SNe (Shen et al. 2010) and nickel-free SN models (Kleiser & Kasen 2014). The spectra are corrected for Milky Way and host extinction. The *x*-axis represents the rest wavelength. The He I and Ca II emission lines are shown in dashed vertical lines. The telluric absorption features are indicated by the ⊕ symbol.

However, such models are inconsistent (too bright) at later times and inconsistent with the overall decay rate.

3.6.2. Analytical Modeling

The bolometric luminosity declines at a rapid rate for the first ∼6 days after peak (see Figure 4). Radioactivity alone is unable to power this early-time luminosity under the constraint that the ejecta mass must be greater than the nickel mass. The peak luminosity of 2.5×10^{42} erg s^{-1} and timescale of evolution (≈4.9 days) falls in the forbidden region of nickel-powered lightcurves (see Figure 1 in Kasen 2017). Instead, we model this early lightcurve as being powered by shock-cooling

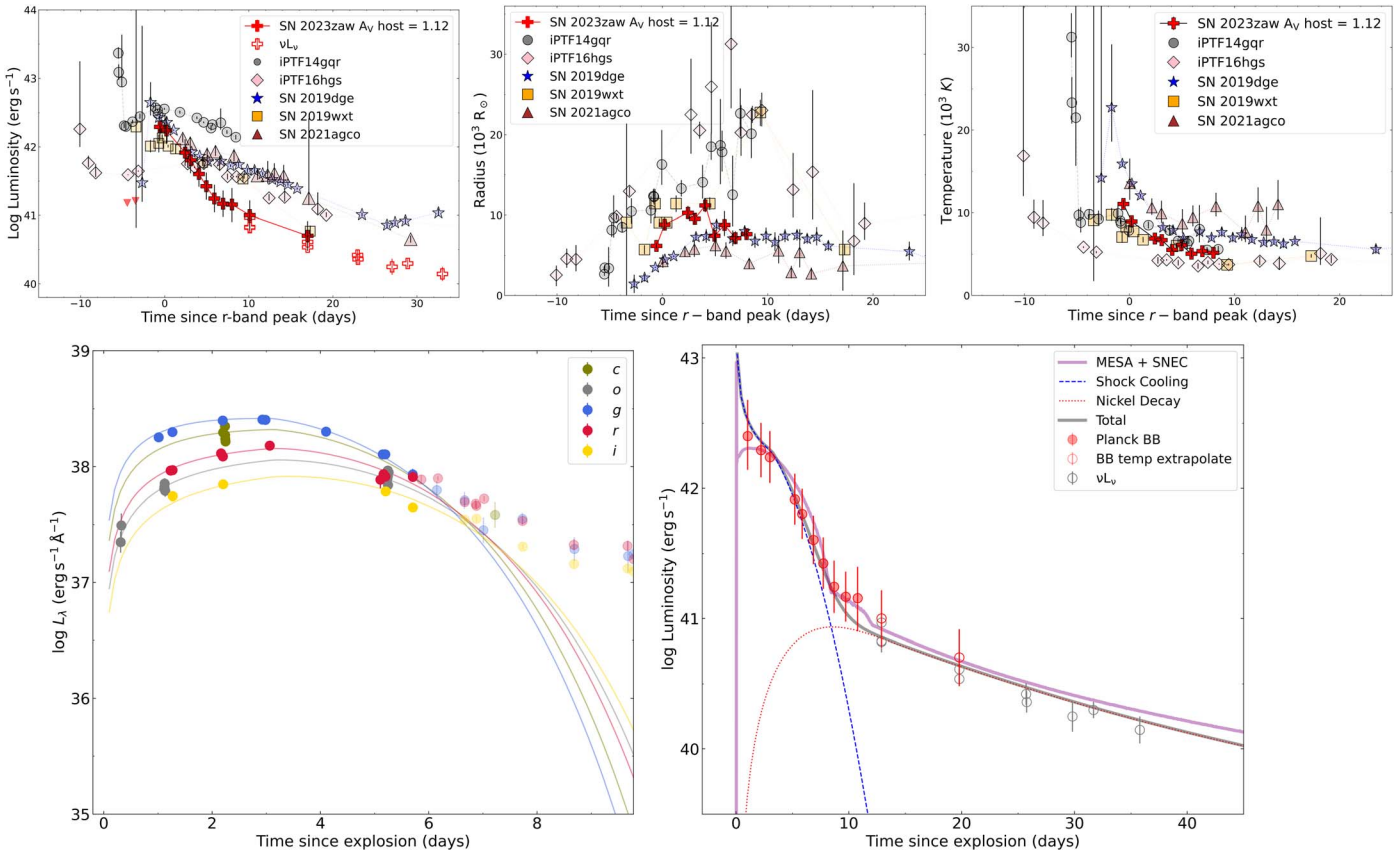

Figure 4. Top: comparison of the bolometric luminosity, best-fit radius, and temperature evolution of SN 2023zaw from the blackbody fits described in Section 3.5 with ultrastripped SN candidates—SN 2019dge (Yao et al. 2020), iPTF14gqr (De et al. 2018b), SN 2019wxt (Agudo et al. 2023; Shivkumar et al. 2023), and SN 2022agco (Yan et al. 2023). Bottom left: shock-cooling-emission model fit to the early-phase multiband lightcurve as described in Section 3.6.2. Bottom right: best-fits for bolometric luminosity with radiation-hydrodynamics and analytical models as described in Section 3.6.

emission from the shock-heated bound or unbound extended stellar material. We use the shock-cooling-emission model presented in Piro et al. (2021) to fit the early-time multiband photometry. We obtain a good fit for all the filters for photometry up to 6 days past peak (Figure 4). The explosion time is constrained to be -2.7 ± 0.2 days before the peak. Based on the fit, we find that the best-fit envelope mass is $0.20 \pm 0.01\,M_\odot$ and envelope radius is $55 \pm 11\,R_\odot$. This is comparable to the envelope properties measured from shock-cooling-emission modeling in other Type Ibc SNe (see Figure I1). The envelope properties of SN 2023zaw are also consistent with theoretical models for bound and unbound stellar material (Figure I2).

For estimating the Ni mass, we first subtract the contribution of the shock-cooling emission estimated above from the bolometric luminosity, which we then assume to be entirely powered by radioactive decay. We use the analytical expression for a Ni-powered bolometric lightcurve provided in Arnett et al. (1989), Valenti et al. (2008), and Wheeler et al. (2015). Further details on the model fitting can be found in Yao et al. (2020, their Appendix B). Based on the fit, we find that the required Ni mass to power the SN is $0.24 \pm 0.14 \times 10^{-2}\,M_\odot$. We measure a photon diffusion timescale (τ_m) of $6.21^{+0.11}_{-0.11}$ days and characteristic γ-ray diffusion timescale (t_o) of $36.04^{+3.41}_{-2.74}$ days.

We assume that the photospheric velocity is $\sim$12,000 km s^{-1}, as assumed from the He I absorption lines in the ALFOSC spectrum taken at r-band peak. We use an opacity (κ) value of 0.07 cm^2 g^{-1}, appropriate for H-poor SNe (Taddia et al. 2018). We estimate the ejecta mass using the following relation: $\tau_m = \left(\frac{2\kappa M_{\rm ej}}{13.8 c v_{\rm phot}}\right)^{1/2}$, which gives $M_{\rm ej} \approx 0.52^{+0.02}_{-0.02} \times \left(\frac{v_{\rm phot}}{12{,}000\ {\rm km\ s^{-1}}}\right) M_\odot$. The calculated explosion kinetic energy is $\approx 4.82^{+0.18}_{-0.18} \times 10^{50}$ erg s^{-1}.

These explosion parameters are an order of magnitude lower than for regular Type Ibc SNe. The estimated ejecta mass is comparable to other ultrastripped SNe in the literature, while the Ni mass is smaller by a factor of $\sim$5. The rapid lightcurve decline is explained by the low ejecta mass, which allows γ-rays to escape already a few days after the peak. Overall, SN 2023zaw occupies a unique location in the phase-space plot of nickel mass versus ejecta mass (see Figure 5). For comparison, we also plot the nickel and ejecta masses estimated for a sample of stripped-envelope SNe from Taddia et al. (2018) and double-peaked Type Ibc SNe from Das et al. (2023b). We note that the double-peaked SN 2021inl (Jacobson-Galán et al. 2022; Das et al. 2023b) is the other SN with Ni mass $<0.01\,M_\odot$.

We also use the analytical models given in Khatami & Kasen (2019) to obtain a nickel mass estimate of $\approx 2.5 \times 10^{-2}\,M_\odot$ and an ejecta mass estimate of $\approx 0.45\,M_\odot$.

3.7. Host Galaxy Environment

We observed SN 2023zaw and its immediate environment with the integral-field unit KCWI (Section 2.3). These data

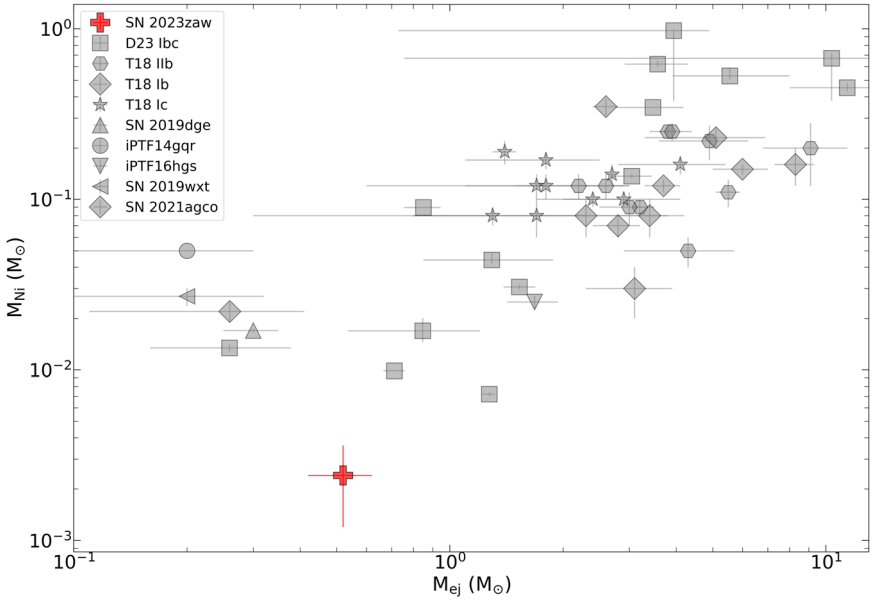

Figure 5. We compare the estimated ejecta mass and nickel mass with Type Ibc SNe from Taddia et al. (2018), double-peaked Type Ibc SNe from Das et al. (2023b) and other ultrastripped SN candidates—SN 2019dge (Yao et al. 2020), iPTF14gqr (De et al. 2018b), SN 2019wxt (Agudo et al. 2023; Shivkumar et al. 2023), and SN 2022agco (Yan et al. 2023). The red plus sign denotes the best-fit parameters by fitting shock-cooling emission + nickel decay to the lightcurve after host-extinction correction.

allow us to address two outstanding questions: (i) Did SN 2023zaw explode in a star-forming region, and (ii) how high is the host attenuation along the line of sight toward SN 2023zaw?

We cleanly detect emission lines from a star-forming region at the SN position in the unbinned KCWI data. To measure the properties of the star-forming region, we extract the SN spectrum using a 4×4 px aperture, tie the flux scale to our g- and i-band photometry, and extract the flux of Hα–Hγ, [O II] $\lambda\lambda$3729, 3729, [O III]$\lambda\lambda$4959, 5007, [N II]$\lambda\lambda$6548, 6584, and [S II]$\lambda\lambda$6717, 6731 by fitting each line with a Gaussian. All measurements are summarized in Table B1.

We infer the attenuation by ionized gas from the flux ratio between Hβ and Hγ (Momcheva et al. 2013). Using the Calzetti et al. (2000) attenuation model, we measure $E(B-V)_{\rm gas} = 0.58 \pm 0.20$ mag, which translates to a stellar continuum color excess of 0.26 ± 0.09 mag. This value is comparable to the reddening inferred from the Na I D absorption lines (Section 3.1) and corroborates that the line of sight is suffering from significant host attenuation.

We note that the stellar populations near SN 2023zaw are evolved and their spectra show conspicuous Balmer absorption lines. This could introduce a bias into the observed Balmer decrement. To quantify the impact, we center a box annulus on the SN position and extract a spectrum from the blue KCWI data between 2 and 4 px from the SN position. We fit the stellar continuum with the stellar population fitting code FIREFLY version 1.0.3 (Wilkinson et al. 2017; Neumann et al. 2022), utilizing the stellar population models from Maraston et al. (2020) and assuming the Kroupa initial mass function (IMF), a spectral resolution of 1000–1250 appropriate for our spectroscopic observation (Morrissey et al. 2018), and a velocity dispersion of 130 ± 20 km s^{-1}. The best-fit yields an $E(B-V)_{\rm star}$ of 0.36 mag, comparable to the value at the explosion site. Henceforth, we use $E(B-V)_{\rm gas} = 0.58 \pm 0.20$ mag to characterize the properties of the star-forming region further.

The attenuation-corrected Hα flux of 1.2×10^{-14} erg cm^{-2} s^{-1} translates to a star formation rate (SFR) of $1.4^{+1.2}_{-0.6} \times 10^{-2}\, M_\odot$ yr^{-1} utilizing the relationship between the Hα luminosity and the SFR from Kennicutt (1998) and the scaling factor from Madau & Dickinson (2014) to convert from the Salpeter to the Chabrier IMF in the Kennicutt (1998) relation. The error estimate includes the uncertainty of the flux measurements, the gas-phase attenuation, and the luminosity distance of SN 2023zaw's host galaxy. We stress that the large SFR error reflects the uncertainty in the attenuation correction, not a low precision of the Hα flux measurement (Table B1).

Detecting emission lines from hydrogen, nitrogen, and oxygen also allows us to measure the metallicity of the star-forming region. Using the O3N2 metallicity indicator and the calibration from Curti et al. (2017), we infer a metallicity of 1.18 ± 0.02 solar (statistical error), adopting a solar oxygen abundance of 8.67 (Asplund et al. 2009).

Next, we draw our attention to SN 2023zaw's neighborhood. Figure 1 shows a map of the star formation activity out to a distance of 6.7 kpc from SN 2023zaw's location. This image was generated from the KCWI data. First, we extracted a 20 Å wide image centered on the wavelength of Hα. Then, we extracted two additional 20 Å wide images from emission-line-free regions adjacent to Hα and interpolated between them to remove the galaxy/SN flux at the wavelength of Hα. Finally, the intensity scale was corrected for MW extinction, scaled to the SN photometry, and converted to SFR as we did for the explosion site. The SFRs in Figure 1 are strict lower limits. They account for neither host attenuation nor stellar Balmer absorption lines.

The explosion site, marked by the blue circle in Figure 1, is located near the outskirts of a larger region with ongoing star formation activity. Although the level of star formation activity at the explosion site is in the lower half of the intensity

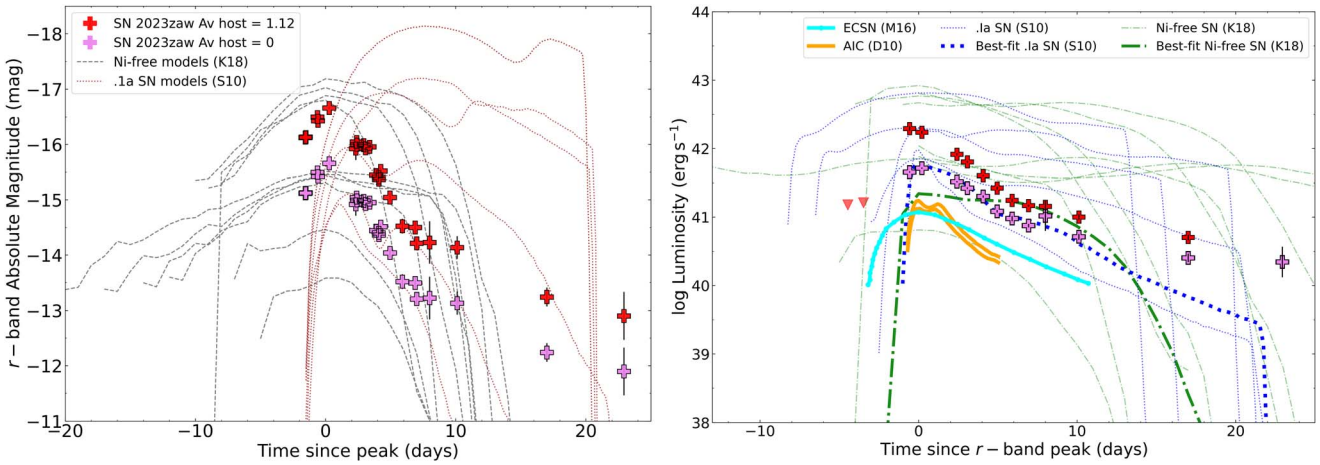

Figure 6. Comparison of the *r*-band and bolometric luminosity of SN 2023zaw with theoretical models for ".Ia" SNe (Shen et al. 2010), nickel-free SNe (Kleiser et al. 2018), ECSN (Moriya & Eldridge 2016), and AIC of WD (Darbha et al. 2010). The bold blue and green lines indicate the best-fit ".Ia" and nickel-free SN models, respectively.

distribution, this star-forming region extends much farther. Inspecting the neighboring spaxels reveals that the star formation activity extends to regions of even less intensity. Thus, the location of SN 2023zaw favors a massive star progenitor, but it does not rule out a thermonuclear origin.

4. Discussion: Progenitor and Evolutionary Pathways

In this section, we discuss the possible progenitors and evolutionary pathways for SN 2023zaw.

4.1. Thermonuclear ".Ia" SN

In the ".Ia" SN scenario, the progenitor is a WD in a close binary ($P_{\rm orb} < 1$ hr) system, accreting helium from its companion. They have a tenth of the ejecta mass and explosion energy of a normal Type Ia SN (Bildsten et al. 2007). We compare the *r*-band lightcurve and bolometric luminosity with ".Ia" SN models from Shen et al. (2010) in Figure 6. The peak luminosities range from 0.5 to 5×10^{42} erg s^{-1} or peak-bolometric magnitudes from −15.5 to −18 mag, consistent with SN 2023zaw. We highlight the best-fit ".Ia" SN bolometric lightcurve, which is an excellent fit to the early-time data before host-extinction correction. Prominent He I features from unburnt He are predicted, which is consistent with the spectra of SN 2023zaw. We note that the absence of broad O I λ7774 and the presence of Ca II NIR lines at early phases resemble the spectra of SN 2010X (Kasliwal et al. 2010), which is a ".Ia" SN candidate (see Figure 3). However, the fact that the decline of the *r*-band lightcurve slows down after ∼10 days postpeak is not consistent with the ".Ia" SN models (Shen et al. 2010).

4.2. AIC of a WD

O–Ne WDs collapse to form an NS when it approaches Chandrasekhar mass. Numerical simulations predict very low explosion energy ($\sim 0.5 \times 10^{49}$ erg). We compare the bolometric lightcurve prediction from Darbha et al. (2010) with SN 2023zaw in Figure 6. The predicted peak luminosity is ∼10 times fainter than that observed for SN 2023zaw. The models do not predict the late-time tail seen in SN 2023zaw. The nickel mass predicted in AIC models ($\lesssim 0.001\,M_\odot$) is slightly smaller than that estimated for SN 2023zaw. The ejecta velocities predicted for AIC explosions are very high (∼0.1*c*), which is not consistent with SN 2023zaw.

4.3. WD–NS/Black Hole Merger

Spectroscopic models of WD–NS/black hole (BH) mergers (Gillanders et al. 2020) predict that the ejecta should be rich in intermediate elements such as O, Mg, and S. This is not consistent with the observed spectra for SN 2023zaw.

4.4. Nickel-free Core-collapse SN

A potential powering mechanism for a fast-evolving, low-Ni mass SN is the "Ni-free" SN scenario (Kleiser & Kasen 2014; Kleiser et al. 2018). In this case, the SN is not powered by decay of radionuclides like ^{56}Ni but is instead powered by shock interactions with an extended hydrogen-poor CSM. We compare the *r*-band lightcurve and bolometric luminosity of SN 2023zaw with Ni-free SN models from Kleiser et al. (2018) in Figure 6. If there is a significant amount of Ni present ($>0.05\,M_\odot$), it shows up as a second peak in the model lightcurves, which is not seen for SN 2023zaw. The models with 0 or $0.01\,M_\odot$ of nickel produce bright and short-lived peaks. However, none of the lightcurves can explain the rapid rise and the slower-evolving late-time lightcurve tail of SN 2023zaw.

4.5. ECSN

The low nickel mass is consistent with super–asymptotic giant branch (sAGB) progenitor stars with an O–Ne–Mg core that explodes as an ECSN. However, an sAGB star has a hydrogen-rich envelope. Since, the spectra do not show hydrogen, a binary system is necessary, where the hydrogen has been stripped off through Roche-lobe overflow or common envelope ejection. Stripped-envelope ECSN models in Moriya & Eldridge (2016) predict ejecta mass of $\sim 0.3-0.6\,M_\odot$, nickel mass of $\sim 0.003\,M_\odot$, and explosion energy of 10^{50} erg, which is consistent with SN 2023zaw. Enhanced production of calcium is predicted for these SN, which is also consistent with the

Table 1
Comparison of Explosion Properties of SN 2023zaw

Source	Redshift	Host Type	r-band Peak (mag)	M_{ej} ($M_\odot$)	M_{Ni} (10^{-2} $M_\odot$)	R_{ext} (10^{13} cm)	M_{ext} (10^{-2} $M_\odot$)
SN 2023zaw	0.0101	Spiral	-16.7 ± 0.1	$0.52^{+0.02}_{-0.02}$	$0.24^{+0.02}_{-0.02}$	$0.4^{+0.1}_{-0.1}$	$19.53^{+0.99}_{-0.98}$
SN 2021agco	0.01056	Spiral	-16.2 ± 0.24	$0.26^{+0.04}_{-0.02}$	$2.2^{+0.2}_{-0.3}$	$0.55^{+0.18}_{-0.14}$	$10.04^{+1.87}_{-1.05}$
AT 2019wxt	0.036	Compact	-16.6 ± 0.4	$0.20^{+0.12}_{-0.11}$	$2.7^{+0.33}_{-0.18}$	$35.8^{+4.06}_{-3.68}$	$3.55^{+0.12}_{-0.11}$
SN 2019dge	0.021	Compact	-16.3 ± 0.2	$0.30^{+0.02}_{-0.02}$	$1.6^{+0.04}_{-0.03}$	$1.2^{+0.06}_{-0.05}$	$9.71^{+0.28}_{-0.27}$
iPTF14gqr	0.063	Spiral	-17.5 ± 0.2	$0.20^{-0.10}_{+0.10}$	$5.0^{+0.14}_{-0.15}$	$6.1^{+8.73}_{-3.18}$	$2.59^{+0.46}_{-0.34}$
iPTF16hgs	0.017	Spiral	-15.5 ± 0.2	$1.68^{+0.28}_{-0.25}$	$2.5^{+0.20}_{-0.22}$	$2.6^{+14.08}_{-1.80}$	$9.27^{+3.40}_{-2.48}$

Note. Comparison of explosion properties of SN 2023zaw with ultrastripped SN candidates — SN 2019dge (Yao et al. 2020), iPTF14gqr (De et al. 2018b), iPTF16hgs (De et al. 2018a), SN 2019wxt (Agudo et al. 2023; Shivkumar et al. 2023), and SN 2022agco (Yan et al. 2023).

broad Ca emission lines seen in SN 2023zaw, as early as 2 days after peak. We compared the theoretical lightcurves from Moriya & Eldridge (2016) with SN 2023zaw in Figure 6. The predicted peak-bolometric luminosities ($\sim 10^{41}$ erg s^{-1}) are $\sim$10 times fainter than the peak luminosity measured for SN 2023zaw.

4.6. Ultrastripped Core-collapse SN from a Low-mass Progenitor Embedded in a He-rich CSM

An ultrastripped SN (Tauris et al. 2015) is a possible channel for the formation of double-NS systems. They arise from a binary star system where a He star undergoes a high degree of stripping by its smaller companion, such that the remaining ejecta mass is $<1\,M_\odot$. The nickel mass is also expected to be quite low ($\sim 0.01\,M_\odot$). Due to the low nickel and ejecta mass, the lightcurves are expected to be faint and show fast evolution. The multiband lightcurve and bolometric properties of SN 2023zaw are consistent with an ultrastripped SN scenario (Figures 2, 4, and G1). We compare the measured ejecta and nickel mass for SN 2023zaw with other ultrastripped SN candidates in the literature in Table 1 and Figure 5. The estimated ejecta mass is comparable with other ultrastripped SN candidates, while the nickel mass is a factor of $\sim$5 lower. We could also reproduce the observed lightcurve by using ultrastripped SN progenitor models evolved with MESA and exploded using SNEC (see Section 3.6.1).

4.6.1. Implication of Narrow He I Lines in the Late-time Spectra

The presence of narrow He I emission lines in the late-time spectra at 30 and 60 days post-peak implies the presence of a He-rich dense CSM shell, which is consistent with the predictions of ultrastripped SN models. We note that we do not see prominent narrow He I emission lines in the spectra taken prior to 9 days after peak. It is likely the broad He I lines from the ejecta dominate over the narrow CSM emission lines in the initial days. But if there is actually no CSM interaction until +8 days, we can constrain the CSM shell to be at $\sim 10^{15}$ cm, which is consistent with the short-period binary models from Wu & Fuller (2022). While the mass-transfer model in Wu & Fuller (2022) assumes that the stellar material lost through the L2 point is distributed spherically, a torus-like distribution of the CSM is also likely (Pejcha et al. 2016; Lu et al. 2023). The viewing angle will strongly influence the observed spectral line widths. In this scenario, the early spectra do not show narrow lines as the CSM is engulfed in the SN ejecta, similar to the model described in Andrews & Smith (2018) for iPTF14hls. Once the photosphere recedes, the CSM is accelerated by the collision of the ejecta to intermediate velocities of $\approx$1000 km s^{-1}. In this scenario, the absence of narrow lines in the ALFOSC spectrum taken at +0 day can be explained if the CSM is confined within 10^{14} cm, which is consistent with the majority of binary mass-transfer models in Wu & Fuller (2022). We note that the CSM interaction does not show up as an additional bump in the optical lightcurve. This could be explained by a very low-mass, He-rich CSM, which is consistent with the estimated low progenitor and ejecta masses. If CSM interaction does contribute significantly to the luminosity, the nickel mass we estimate should be considered as an upper limit.

4.6.2. Implication of Very Low Nickel Mass

Observations and parameterized 1D models of massive star explosions suggest that typically $\sim 0.05\,M_\odot$ Ni should be ejected from a core-collapse SN. Anderson (2019) and Meza & Anderson (2020) measured the Ni mass for a sample of Type II and Type Ibc SNe in the literature and found that the Ni mass synthesized in SESNe was significantly higher than for Type II SNe. The lowest Ni mass in their Type Ibc sample was $0.015\,M_\odot$, and 25% of all Type II SNe has a Ni mass below this limit. However, this might be due to an observational bias as low-Ni-mass SESNe are harder to detect as they are likely to be faint as well as fast evolving. The extremely low amount of Ni mass in SN 2023zaw ($\sim 0.002\,M_\odot$) could imply a fallback event, where most of the Ni produced in the core-collapse immediately fall into the newly formed BH (Turatto et al. 1998; Balberg et al. 2000; Sollerman 2002). However, the observed high velocities do not favor this scenario.

The other explanation is that the progenitor's initial mass lies in the low-mass end of core-collapse SN progenitors, as stars with low-mass iron cores produce a low amount of Ni. Stockinger et al. (2020) and Sandoval et al. (2021) obtained $\sim$0.002–0.005 $M_\odot$ Ni mass for a 9.6 $M_\odot$ progenitor. More recent 3D simulations (Burrows et al. 2024) estimate 0.002–0.006 $M_\odot$ Ni mass for a 9 $M_\odot$ zero-age main-sequence mass progenitor and $>0.01\,M_\odot$ for progenitors with initial mass greater than 9.25 $M_\odot$. We note that these models are not for stripped-envelope SNe. However, if they undergo mass loss after He-core burning, the core evolution of a star is decoupled from the envelope evolution and the nickel mass is expected to be the same. The amount of Ni synthesized in ultrastripped models for low-mass CO stars is $\lesssim 0.01\,M_\odot$ (Moriya et al. 2017; Sawada et al. 2022), which is consistent with our estimate for SN 2023zaw.

5. Conclusion

In this Letter, we have presented the observations and analysis of an unusual stellar explosion—SN 2023zaw. It has the lowest nickel mass among all stripped-envelope SNe discovered so far. SN 2023zaw also shows the fastest evolution among all stripped-envelope SNe, with a time above half maximum of 4.9 days in the r band. The photospheric spectra show broad He I emission lines. It also shows broad Ca NIR emission lines as early as 2 days after peak.

We performed radiation-hydrodynamical and analytical modeling of the lightcurve by fitting with a combination of shock-cooling emission and nickel decay. The early-time lightcurve fits well with shock-cooling emission, with an envelope mass of $\approx 0.2\,M_{\odot}$ and an envelope radius of $\approx 50\,R_{\odot}$. The estimated ejecta and nickel masses are $\approx 0.5\,M_{\odot}$ and $\approx 0.002\,M_{\odot}$, respectively.

We interpret SN 2023zaw as an ultrastripped SN from a low-mass He star—a compact object binary. The late-time evolution of the He star results in an extended He-rich envelope. There is also spectral evidence for thick He-rich CSM, likely from pre-SN mass-loss episodes from late-time Roche-lobe overflow. The very low nickel mass, ejecta mass, and explosion energy can only be explained by a progenitor with an initial mass less than around $10\,M_{\odot}$.

The late-time spectra show prominent narrow He I at a FWHM velocity of $\sim 1000\,\mathrm{km\,s^{-1}}$, indicating the presence of He-rich CSM. It is unclear if CSM interaction also provides a powering mechanism for SN 2023zaw. A number of other models for faint and rapidly evolving transients such as the nickel-free SN, AIC, and ECSN were ruled out based on the peak luminosity and the presence of a late-time tail in the lightcurve of SN 2023zaw. The excess luminosity might be explained if the luminosity is boosted by CSM interaction. In this case, the estimated nickel mass should be treated as an upper limit. Including CSM interaction modeling in the future will help conclusively favor or rule out these scenarios. Also, late-time multiwavelength follow-up will provide useful diagnostics in determining the CSM properties, the pre-SN mass-loss mechanism, and the evolutionary channel (Matsuoka & Maeda 2020; Kashiyama et al. 2022).

Spectroscopic modeling is currently missing for most of the theoretical scenarios for producing faint and rapid transients. Detailed modeling is required to explain some unusual spectroscopic features of SN 2023zaw, such as the presence of strong Ca NIR lines close to peak, redshifted component of He I λ5876 emission line, not reaching nebular phase until 30 days in spite of the low ejecta mass, the emergence of narrow He I emission lines, and the absence of [Ca II], [O I], and Ca NIR emission lines in the nebular phase.

The extremely low nickel mass of SN 2023zaw gives rise to the question—What is the lowest nickel mass that is synthesized in a stripped-envelope SN? Current literature shows that the nickel mass measured in stripped-envelope SNe is significantly higher than in Type II SNe (Anderson 2019). It is likely that this is due to an observational bias, as SESNe with low nickel masses are likely to be faint and fast evolving and hence harder to detect, classify, and follow up. SN 2023zaw underscores the existence of this undiscovered population of low nickel mass SESNe ($<0.005\,M_{\odot}$) with progenitor masses in the low-mass end of core-collapse SNe ($<10\,M_{\odot}$). A systematic study of the lowest-nickel-mass stripped-envelope SNe, including their rates and the nickel mass distribution of low-luminosity SESNe, will be explored in future work. Candidates for such low-nickel-mass stripped-envelope SNe include double-peaked Type Ibc SNe such as SN 2021inl (Jacobson-Galán et al. 2022; Das et al. 2023b), rapidly evolving ($t_{1/2,r} < 10$ days) Type IIb SNe (e.g., Das et al. 2023a; Ho et al. 2023; C. Fremling et al. 2024, in preparation), and rapidly declining H-poor SNe such as SN 2020ghq (Q. Wang et al. 2024 in preparation). For SNe with extremely low Ni mass, the shock-cooling emission is likely to dominate over nickel decay. The ultrastripped SNe candidates in the literature show an early luminosity excess that is powered by shock cooling. Future wide-field UV surveys such as ULTRASAT (Sagiv et al. 2014; Shvartzvald et al. 2024), UVEX (Kulkarni et al. 2021), and deep ground-based surveys such as LSST (Ivezić et al. 2019) in synergy with high-cadenced surveys such as ZTF will provide an exciting opportunity to explore this phase space.

Acknowledgments

K.K.D. acknowledges support from the Schwartz Reisman Collaborative Science Program, which is supported by the Gerald Schwartz and Heather Reisman Foundation. We thank the anonymous referee for the valuable comments that improved the quality of the Letter.

M.W.C. acknowledges support from the National Science Foundation with grant Nos. PHY-2308862 and PHY-2117997.

S. S. is partially supported by LBNL Subcontract No. 7707915.

Based on observations obtained with the Samuel Oschin Telescope 48 inch and the 60 inch Telescope at the Palomar Observatory as part of the Zwicky Transient Facility project. ZTF is supported by the National Science Foundation under grant No. AST-2034437 and a collaboration including Caltech, IPAC, the Oskar Klein Center at Stockholm University, the University of Maryland, University of California, Berkeley, the University of Wisconsin at Milwaukee, University of Warwick, Ruhr University, Cornell University, Northwestern University and Drexel University. Operations are conducted by COO, IPAC, and UW.

SED Machine is based upon work supported by the National Science Foundation under grant No. 1106171.

The ZTF forced-photometry service was funded under the Heising-Simons Foundation grant #12540303 (PI: Graham).

The Gordon and Betty Moore Foundation, through both the Data-Driven Investigator Program and a dedicated grant, provided critical funding for SkyPortal.

This research has made use of the NASA/IPAC Extragalactic Database (NED), which is funded by the National Aeronautics and Space Administration and operated by the California Institute of Technology.

The data presented here were obtained in part with ALFOSC, which is provided by the Instituto de Astrofisica de Andalucia (IAA) under a joint agreement with the University of Copenhagen and NOT.

The Liverpool Telescope is operated on the island of La Palma by Liverpool John Moores University in the Spanish Observatorio del Roque de los Muchachos of the Instituto de Astrofisica de Canarias with financial support from the UK Science and Technology Facilities Council. Based on observations made with the Italian Telescopio Nazionale Galileo (TNG) operated on the island of La Palma by the Fundación Galileo Galilei of the INAF (Istituto Nazionale di Astrofisica) at the Spanish Observatorio del Roque de los Muchachos of the Instituto de Astrofisica de Canarias.

The W. M. Keck Observatory is operated as a scientific partnership among the California Institute of Technology, the University of California and the National Aeronautics and

Space Administration. The Observatory was made possible by the generous financial support of the W. M. Keck Foundation. The authors wish to recognize and acknowledge the very significant cultural role and reverence that the summit of Maunakea has always had within the indigenous Hawaiian community. We are most fortunate to have the opportunity to conduct observations from this mountain.

MMT Observatory access was supported by Northwestern University and the Center for Interdisciplinary Exploration and Research in Astrophysics (CIERA).

Data Availability

All the photometric and spectroscopic data used in this work will be made available on GitHub[25] after publication.

The optical photometry and spectroscopy will also be made public through WISeREP, the Weizmann Interactive Supernova Data Repository (Yaron & Gal-Yam 2012).

Appendix A
Timescale–Luminosity Phase Space

In Figure A1, we compare the time above half maximum and peak luminosity of SN 2023zaw with stripped-envelope SNe and other fast-evolving transients in the literature with rise and decline time constraints.

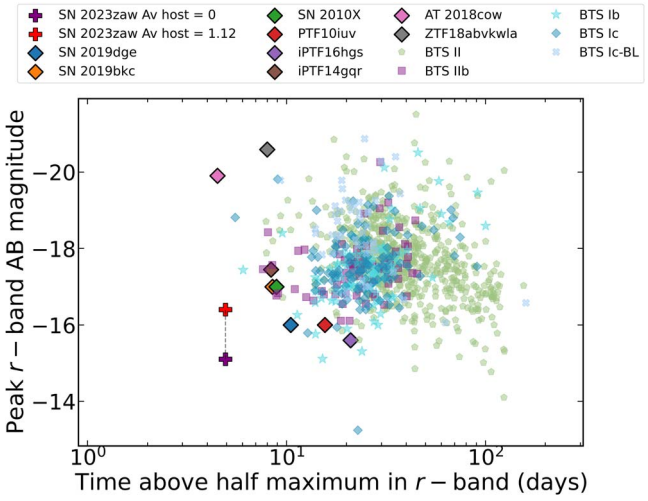

Figure A1. We compare the time above half maximum and peak luminosity of SN 2023zaw with stripped-envelope SNe from the Bright Transient Survey experiment (Perley et al. 2020). For sources with two peaks in the *r*-band lightcurve, the second peak is used. We also compare with other fast-evolving transients—SN 2019dge (Yao et al. 2020), SN 2019bkc (Chen et al. 2020; Prentice et al. 2020), iPTF14gqr (De et al. 2018b), iPTF16hgs (De et al. 2018a), AT 2018cow (Perley et al. 2019), ZTF18abvkwla (Ho et al. 2020).

[25] https://github.com/kaustavkdas/SN2023zaw

Appendix B
Host Galaxy Emission Lines

Table B1 shows the emission-line flux measurements of the star-forming region at the SN site.

Table B1
Emission-line Flux Measurements of the Star-forming Region at the SN Site

Transition	Flux (10^{-17} erg cm^{-2} s^{-1})
[O II] $\lambda\lambda$3726,3729	61.10 ± 5.23
[O III] λ4959	4.63 ± 0.15
[O III] λ5007	13.90 ± 0.46
Hγ	14.83 ± 1.20
Hβ	42.48 ± 2.51
[N II] λ6549	26.04 ± 1.27
Hα	203.98 ± 6.74
[N II] λ6584	78.12 ± 3.81
[S II] λ6718	40.84 ± 1.61
[S II] λ6732	28.69 ± 1.43

Note. No measurement is corrected for reddening.

Appendix C
Photometry Data

A truncated version of the photometry table is shown in Table C1. All the photometric and spectroscopic data used in this work will be made available on GitHub (see footnote 25) after publication.

Table C1
Truncated Photometry Data for SN 2023zaw

MJD	Instrument	Filter	AB Magnitude
60285	ATLAS	*o*	19.33 ± 0.26
60285	P48	*g*	18.34 ± 0.06
60285	ATLAS	*o*	18.16 ± 0.07
60285	SEDM	*r*	18.09 ± 0.07
60285	SEDM	*g*	18.23 ± 0.05
60285	SEDM	*r*	18.08 ± 0.04
60285	SEDM	*i*	17.91 ± 0.06
60286	SEDM	*r*	17.72 ± 0.06
60286	SEDM	*g*	17.98 ± 0.05
60286	SEDM	*r*	17.78 ± 0.04
60286	SEDM	*i*	17.65 ± 0.02
60286	ATLAS	*c*	17.88 ± 0.05
60287	P48	*g*	17.96 ± 0.05
60287	P48	*g*	17.97 ± 0.04

Note. The full machine-readable version will be made available on GitHub (https://github.com/kaustavkdas/SN2023zaw) after publication. The photometry data have been corrected for Milky Way extinction.

(This table is available in its entirety in machine-readable form in the online article.)

Appendix D
Spectroscopy Collage

A collage all the spectra of SN 2023zaw is shown in Figure D1.

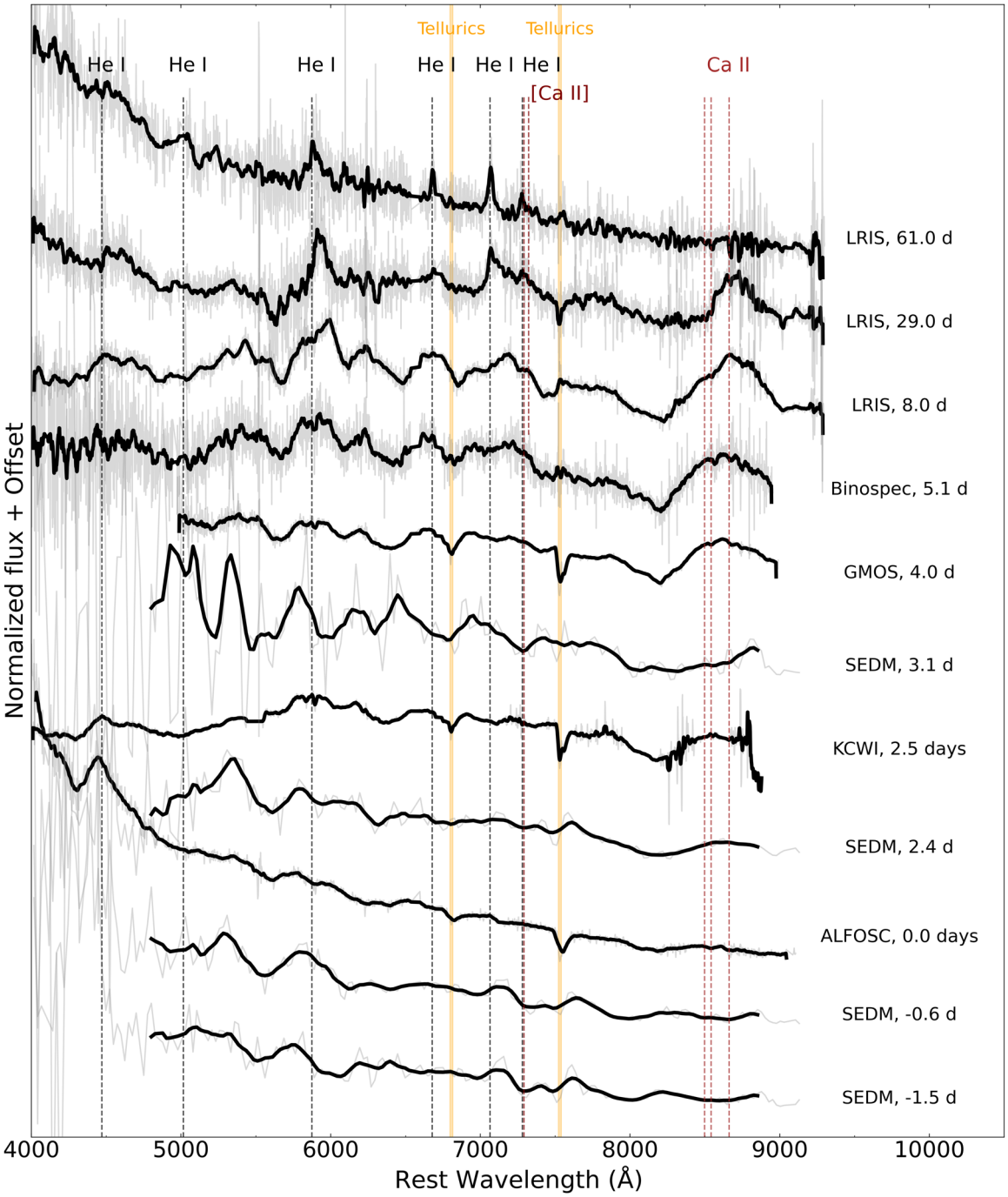

Figure D1. Spectral sequence for SN 2023zaw. The phases are in rest-frame days since the *r*-band peak (MJD = 60287.7). See Section 2.3 for details on the obtained spectra.

Appendix E
Spectroscopy Log

The spectroscopy log is shown in Table E1.

Table E1
Spectroscopy Log

Date	Phase[a]	Instrument
2023 Dec 12	−1.5	SEDM
2023 Dec 8	−0.6	SEDM
2023 Dec 9	0.0	ALFOSC
2023 Dec 11	+2.4	SEDM
2023 Dec 12	+2.5	KCWI
2023 Dec 12	+3.1	SEDM
2023 Dec 13	+4.0	GMOS
2023 Dec 14	+5.1	Binospec
2023 Dec 17	+8.0	LRIS
2024 Jan 7	+29.0	LRIS
2024 Feb 7	+61.0	LRIS

Note.
[a] Days since r-band peak (MJD = 60287.7).

Appendix F
Color Evolution Plot

The $g-r$ and $r-i$ color evolution of SN 2023zaw compared to other SNe in the literature is shown in Figure F1.

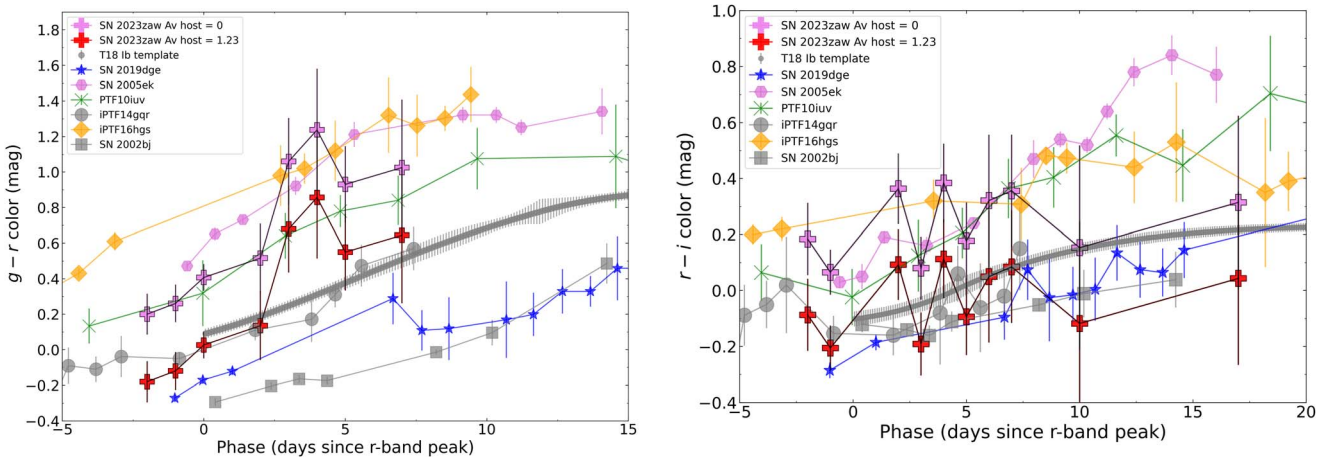

Figure F1. The $g-r$ (left) and $r-i$ (right) color evolution of SN 2023zaw compared to other fast transients—SN 2005ek (Drout et al. 2013), SN 2019dge (Yao et al. 2020), iPTF14gqr (De et al. 2018b), and iPTF14hgs (De et al. 2018a). The gray line shows the intrinsic color template for Type Ib SNe from Stritzinger et al. (2018).

Appendix G
Lightcurve Comparison

In Figure G1, we compare the *r*-band lightcurve of SN 2023zaw with other fast-evolving transients in the literature.

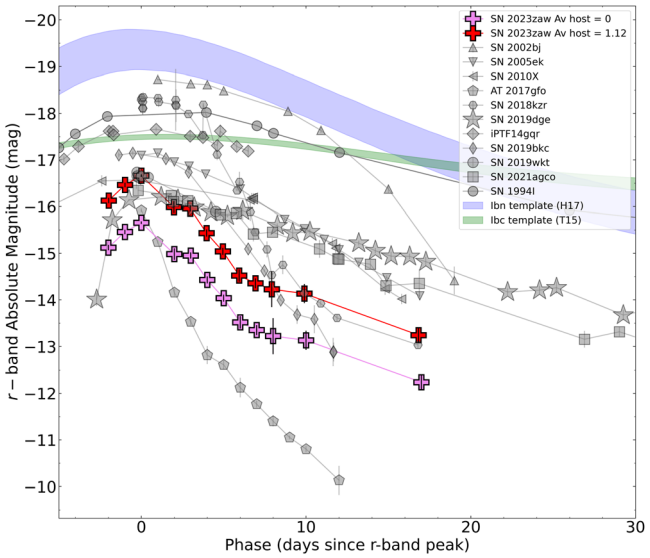

Figure G1. The *r*-band lightcurve of SN 2023zaw compared with other fast-evolving transients in the literature: fast-declining Type I SNe—SN 2010X (Kasliwal et al. 2010) and SN 2019bkc (Chen et al. 2020; Prentice et al. 2020); the kilonova AT 2017gfo (Abbott et al. 2017); ultrastripped SN candidates—SN 2019dge (Yao et al. 2020), iPTF14gqr (De et al. 2018b), SN 2019wxt (Agudo et al. 2023; Shivkumar et al. 2023), and SN 2022agco (Yan et al. 2023).

Appendix H
Blackbody Best-fit Parameters

The summary of the best-fit blackbody properties can be found in Table H1.

Table H1
Summary of the Blackbody Properties for SN 2023zaw

Phase (days)	Log Luminosity (erg s^{-1})	Temperature (K)	Radius ($R_\odot$)
−2	$42.40^{+0.10}_{-0.08}$	15620^{+1850}_{-1440}	3500^{+360}_{-360}
−1	$42.29^{+0.03}_{-0.03}$	11050^{+510}_{-490}	6180^{+340}_{-320}
0	$42.24^{+0.02}_{-0.02}$	8960^{+500}_{-460}	8820^{+760}_{-700}
2	$41.92^{+0.02}_{-0.02}$	6900^{+340}_{-330}	10270^{+860}_{-750}
3	$41.80^{+0.02}_{-0.02}$	6710^{+300}_{-280}	9530^{+710}_{-670}
4	$41.60^{+0.01}_{-0.01}$	5520^{+230}_{-210}	11190^{+880}_{-830}
5	$41.42^{+0.02}_{-0.02}$	6100^{+380}_{-340}	7440^{+790}_{-720}
6	$41.24^{+0.02}_{-0.03}$	5060^{+470}_{-430}	8780^{+1710}_{-1360}
7	$41.17^{+0.02}_{-0.02}$	5370^{+320}_{-290}	7140^{+870}_{-760}
8	$41.16^{+0.07}_{-0.08}$	5160^{+10}_{-10}	7640^{+590}_{-660}
10	$41.00^{+0.04}_{-0.05}$	5070^{+10}_{-10}	6630^{+310}_{-330}
17	$40.70^{+0.04}_{-0.04}$	5000^{+10}_{-10}	4830^{+220}_{-240}

Note. A machine-readable version is available in the electronic edition. A comma-separated values file version is available at https://github.com/kaustavkdas/SN2023zaw/blob/main/lightcurve_23bqun_MW_TableC1.csv.

(This table is available in its entirety in machine-readable form in the online article.)

Appendix I
Comparison of Envelope Properties

We compare the envelope properties of SN 2023zaw with ultra-stripped SNe candidates and Type Ibn SNe in Figure I1. We compare the envelope properties of SN 2023zaw with theoretical models for bound and unbound stellar material in Figure I2.

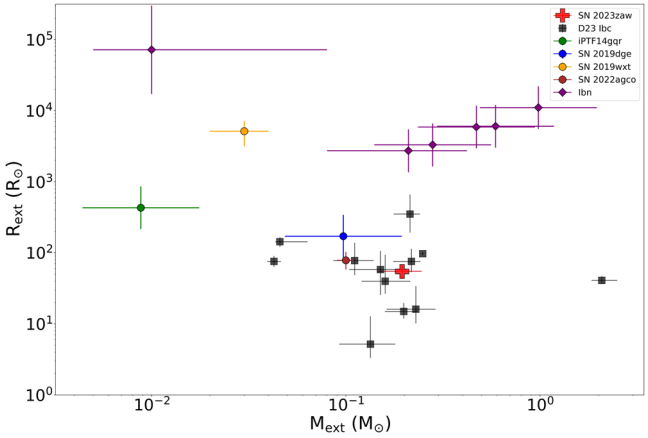

Figure I1. The envelope properties of SN 2023zaw (red cross) compared with double-peaked Type Ibc SNe (black squares) from Das et al. (2023b), USSN candidates (circles)—iPTF14gqr, SN 2019dge, SN 2019wxt, SN 2022agco (De et al. 2018b; Yao et al. 2020; Agudo et al. 2023; Shivkumar et al. 2023; Yan et al. 2023), and Type Ibn SNe (purple diamonds)—SN 2006jc, SN 2019wep, SN 2019up, SN 2012jpk, SN 2019deh, LSQ13ddu (Anupama et al. 2009; Clark et al. 2020; Pellegrino et al. 2022).

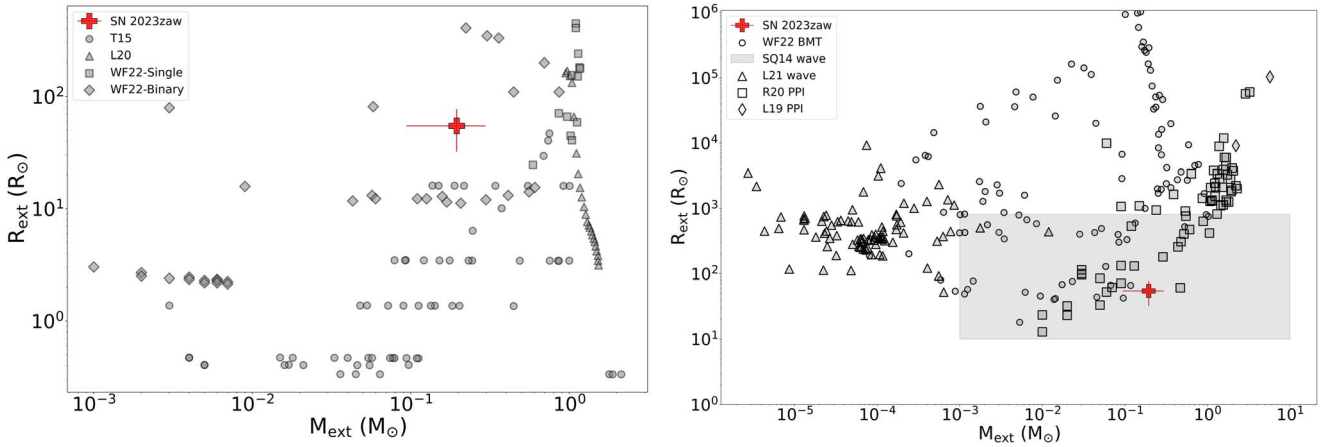

Figure I2. Left: comparison of the envelope properties of SN 2023zaw with theoretical models for bound stellar material—binary and single star models from Wu & Fuller (2022; WF22), Laplace et al. (2020; L20), and Tauris et al. (2015; T15). Right: comparison of the the envelope properties of SN 2023zaw with theoretical models for unbound stellar material—late-time binary mass transfer (BMT; Wu & Fuller 2022), wave-driven mass loss (Shiode & Quataert 2014; Leung et al. 2021), pulsation-pair-instability driven mass loss (PPI; Leung et al. 2019; Renzo et al. 2020).

Appendix J
Priors and Corner Plots

The priors and corner plots for shock-cooling emission and radioactive decay model fitting are shown in Tables J1 and J2, and Figure J1.

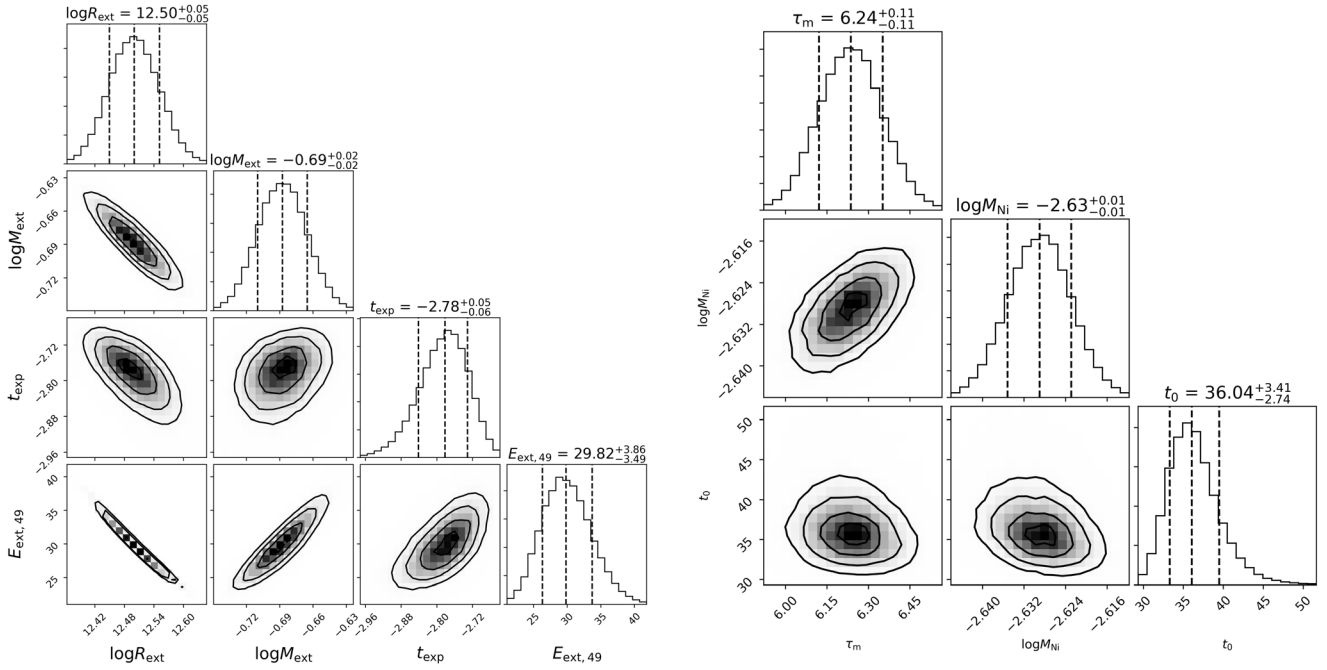

Figure J1. Corner plots showing the posterior constraints of the model parameters in the shock-cooling-emission (left) and radioactive decay (right) models described in Section 3.6.2.

Table J1
Priors Used for Shock-cooling-emission Model Fitting Described in Section 3.6.2

Parameter	Prior
$\log R_{\rm ext}$	$\mathcal{U}(-5, 25)$
$\log M_{\rm ext}$	$\mathcal{U}(-4, 1)$
$E_{\rm ext,49}$	$\mathcal{U}(0.1, 100)$

Table J2
Priors Used for Nickel Decay Model Fitting Described in Section 3.6.2

Parameter	Prior
$\tau_{\rm m}$	$\mathcal{U}(1, 20)$
$\log M_{\rm Ni}$	$\mathcal{U}(-4, 0)$
t_0	$\mathcal{U}(2, 100)$

ORCID iDs

Kaustav K. Das https://orcid.org/0000-0001-8372-997X
Christoffer Fremling https://orcid.org/0000-0002-4223-103X
Mansi M. Kasliwal https://orcid.org/0000-0002-5619-4938
Steve Schulze https://orcid.org/0000-0001-6797-1889
Jesper Sollerman https://orcid.org/0000-0003-1546-6615
Viraj Karambelkar https://orcid.org/0000-0003-2758-159X
Sam Rose https://orcid.org/0000-0003-4725-4481
Shreya Anand https://orcid.org/0000-0003-3768-7515
Igor Andreoni https://orcid.org/0000-0002-8977-1498
Sean J. Brennan https://orcid.org/0000-0003-1325-6235
S. Bradley Cenko https://orcid.org/0000-0003-1673-970X
Michael W. Coughlin https://orcid.org/0000-0002-8262-2924
B. O'Connor https://orcid.org/0000-0002-9700-0036
Kishalay De https://orcid.org/0000-0002-8989-0542
Jim Fuller https://orcid.org/0000-0002-4544-0750
Matthew Graham https://orcid.org/0000-0002-3168-0139
Erica Hammerstein https://orcid.org/0000-0002-5698-8703
Annastasia Haynie https://orcid.org/0000-0003-4287-4577
S. R. Kulkarni https://orcid.org/0000-0001-5390-8563
Chang Liu https://orcid.org/0000-0002-7866-4531
Ashish A. Mahabal https://orcid.org/0000-0003-2242-0244
Christopher Martin https://orcid.org/0000-0002-8650-1644
Adam A. Miller https://orcid.org/0000-0001-9515-478X
James D. Neill https://orcid.org/0000-0002-0466-1119
Daniel A. Perley https://orcid.org/0000-0001-8472-1996
Priscila J. Pessi https://orcid.org/0000-0002-8041-8559
Nikolaus Z. Prusinski https://orcid.org/0000-0001-5847-7934
Josiah Purdum https://orcid.org/0000-0003-1227-3738
Vikram Ravi https://orcid.org/0000-0002-7252-5485
Ben Rusholme https://orcid.org/0000-0001-7648-4142
Samantha Wu https://orcid.org/0000-0003-2872-5153
Avery Wold https://orcid.org/0000-0002-9998-6732
Lin Yan https://orcid.org/0000-0003-1710-9339

References

Abbott, B. P., Abbott, R., Abbott, T. D., et al. 2017, PhRvL, 119, 161101
Agudo, I., Amati, L., An, T., et al. 2023, A&A, 675, A201
Anderson, J. P. 2019, A&A, 628, A7
Andreoni, I., Coughlin, M. W., Kool, E. C., et al. 2021, ApJ, 918, 63
Andrews, J. E., & Smith, N. 2018, MNRAS, 477, 74
Anupama, G. C., Sahu, D. K., Gurugubelli, U. K., et al. 2009, MNRAS, 392, 894
Arnett, W. D., Bahcall, J. N., Kirshner, R. P., & Woosley, S. E. 1989, ARA&A, 27, 629
Asplund, M., Grevesse, N., Sauval, A. J., & Scott, P. 2009, ARA&A, 47, 481
Balberg, S., Zampieri, L., & Shapiro, S. L. 2000, ApJ, 541, 860
Bellm, E. C., Kulkarni, S. R., Graham, M. J., et al. 2019, PASP, 131, 018002
Bildsten, L., Shen, K. J., Weinberg, N. N., & Nelemans, G. 2007, ApJL, 662, L95
Blagorodnova, N., Neill, J. D., Walters, R., et al. 2018, PASP, 130, 035003
Blondin, S., & Tonry, J. L. 2007, ApJ, 666, 1024
Burrows, A., Wang, T., & Vartanyan, D. 2024, ApJL, 964, L16
Calzetti, D., Armus, L., Bohlin, R. C., et al. 2000, ApJ, 533, 682
Cardelli, J. A., Clayton, G. C., & Mathis, J. S. 1989, ApJ, 345, 245
Cenko, S. B., Fox, D. B., Moon, D.-S., et al. 2006, PASP, 118, 1396
Chambers, K. C., Magnier, E. A., Metcalfe, N., et al. 2016, arXiv:1612.05560
Chen, P., Dong, S., Stritzinger, M. D., et al. 2020, ApJL, 889, L6
Clark, P., Maguire, K., Inserra, C., et al. 2020, MNRAS, 492, 2208
Curti, M., Cresci, G., Mannucci, F., et al. 2017, MNRAS, 465, 1384
Darbha, S., Metzger, B. D., Quataert, E., et al. 2010, MNRAS, 409, 846
Das, K. K., Kasliwal, M. M., Fremling, C., et al. 2023a, ApJ, 959, 12
Das, K. K., Kasliwal, M. M., Sollerman, J., et al. 2023b, arXiv:2306.04698
De, K., Kasliwal, M. M., Cantwell, T., et al. 2018a, ApJ, 866, 72
De, K., Kasliwal, M. M., Ofek, E. O., et al. 2018b, Sci, 362, 201
De, K., Kasliwal, M. M., Tzanidakis, A., et al. 2020, ApJ, 905, 58
Dekany, R., Smith, R. M., Riddle, R., et al. 2020, PASP, 132, 038001
Dessart, L., Burrows, A., Livne, E., & Ott, C. D. 2007, ApJ, 669, 585
Drout, M. R., Soderberg, A. M., Mazzali, P. A., et al. 2013, ApJ, 774, 58
Fabricant, D., Fata, R., Epps, H., et al. 2019, PASP, 131, 075004
Foley, R. J., Smith, N., Ganeshalingam, M., et al. 2007, ApJL, 657, L105
Foreman-Mackey, D., Hogg, D. W., Lang, D., & Goodman, J. 2013, PASP, 125, 306
Fremling, C., Miller, A. A., Sharma, Y., et al. 2020, ApJ, 895, 32
Fremling, C., Sollerman, J., Kasliwal, M. M., et al. 2018, A&A, 618, A37
Fremling, C., Sollerman, J., Taddia, F., et al. 2016, A&A, 593, A68
Gillanders, J. H., Huber, M., Chambers, K., et al. 2023, TNSAN, 341, 1
Gillanders, J. H., Sim, S. A., & Smartt, S. J. 2020, MNRAS, 497, 246
Graham, M. J., Kulkarni, S. R., Bellm, E. C., et al. 2019, PASP, 131, 078001
Ho, A. Y. Q., Perley, D. A., Gal-Yam, A., et al. 2023, ApJ, 949, 120
Ho, A. Y. Q., Perley, D. A., Kulkarni, S. R., et al. 2020, ApJ, 895, 49
Hosseinzadeh, G., Arcavi, I., Valenti, S., et al. 2017, ApJ, 836, 158
Ivezić, Ž., Kahn, S. M., Tyson, J. A., et al. 2019, ApJ, 873, 111
Jacobson-Galán, W. V., Venkatraman, P., Margutti, R., et al. 2022, ApJ, 932, 58
Kasen, D. 2017, in Handbook of Supernovae, ed. A. W. Alsabti & P. Murdin (Berlin: Springer), 939
Kashiyama, K., Sawada, R., & Suwa, Y. 2022, ApJ, 935, 86
Kasliwal, M. M., Kulkarni, S. R., Gal-Yam, A., et al. 2010, ApJL, 723, L98
Kennicutt, R. C., Jr. 1998, ARA&A, 36, 189
Khatami, D. K., & Kasen, D. N. 2019, ApJ, 878, 56
Kim, Y. L., Rigault, M., Neill, J. D., et al. 2022, PASP, 134, 024505
Kleiser, I. K. W., & Kasen, D. 2014, MNRAS, 438, 318
Kleiser, I. K. W., Kasen, D., & Duffell, P. C. 2018, MNRAS, 475, 3152
Kulkarni, S. R., Harrison, F. A., Grefenstette, B. W., et al. 2021, arXiv:2111.15608
Laplace, E., Götberg, Y., de Mink, S. E., Justham, S., & Farmer, R. 2020, A&A, 637, A6
Leung, S.-C., Fuller, J., & Nomoto, K. 2021, ApJ, 915, 80
Leung, S.-C., Nomoto, K., & Blinnikov, S. 2019, ApJ, 887, 72
Lu, W., Fuller, J., Quataert, E., & Bonnerot, C. 2023, MNRAS, 519, 1409
Madau, P., & Dickinson, M. 2014, ARA&A, 52, 415
Maraston, C., Hill, L., Thomas, D., et al. 2020, MNRAS, 496, 2962
Margalit, B., & Metzger, B. D. 2016, MNRAS, 461, 1154
Martin, C., Moore, A., Morrissey, P., et al. 2010, Proc. SPIE, 7735, 77350M
Masci, F. J., Laher, R. R., Rusholme, B., et al. 2019, PASP, 131, 018003
Matsuoka, T., & Maeda, K. 2020, ApJ, 898, 158
McBrien, O. R., Smartt, S. J., Chen, T.-W., et al. 2019, ApJL, 885, L23
Meza, N., & Anderson, J. P. 2020, A&A, 641, A177
Momcheva, I. G., Lee, J. C., Ly, C., et al. 2013, AJ, 145, 47
Moriya, T., Tominaga, N., Tanaka, M., et al. 2010, ApJ, 719, 1445
Moriya, T. J., & Eldridge, J. J. 2016, MNRAS, 461, 2155
Moriya, T. J., Mazzali, P. A., Tominaga, N., et al. 2017, MNRAS, 466, 2085
Morozova, V., Piro, A. L., Renzo, M., et al. 2015, ApJ, 814, 63
Morrissey, P., Matuszewski, M., Martin, D. C., et al. 2018, ApJ, 864, 93
Mould, J. R., Huchra, J. P., Freedman, W. L., et al. 2000, ApJ, 529, 786
Neumann, J., Thomas, D., Maraston, C., et al. 2022, MNRAS, 513, 5988
Oke, J. B., Cohen, J. G., Carr, M., et al. 1995, PASP, 107, 375
Paxton, B., Bildsten, L., Dotter, A., et al. 2010, MESA: Modules for Experiments in Stellar Astrophysics, Astrophysics Source Code Library, ascl:1010.083
Pejcha, O., Metzger, B. D., & Tomida, K. 2016, MNRAS, 461, 2527
Pellegrino, C., Howell, D. A., Terreran, G., et al. 2022, ApJ, 938, 73
Perley, D. A. 2019, PASP, 131, 084503
Perley, D. A., Fremling, C., Sollerman, J., et al. 2020, ApJ, 904, 35
Perley, D. A., Mazzali, P. A., Yan, L., et al. 2019, MNRAS, 484, 1031
Phillips, M. M., Simon, J. D., Morrell, N., et al. 2013, ApJ, 779, 38
Piro, A. L., Haynie, A., & Yao, Y. 2021, ApJ, 909, 209
Poznanski, D., Ganeshalingam, M., Silverman, J. M., & Filippenko, A. V. 2011, MNRAS, 415, L81
Poznanski, D., Prochaska, J. X., & Bloom, J. S. 2012, MNRAS, 426, 1465
Prentice, S. J., Maguire, K., Flörs, A., et al. 2020, A&A, 635, A186
Prochaska, J. X., Hennawi, J., Cooke, R., et al. 2020a, pypeit/PypeIt: Release v1.0.0, Zenodo, doi:10.5281/zenodo.3743493
Prochaska, J. X., Hennawi, J. F., Westfall, K. B., et al. 2020b, JOSS, 5, 2308
Pursiainen, M., Leloudas, G., Schulze, S., et al. 2023, ApJL, 959, L10
Renzo, M., Farmer, R., Justham, S., et al. 2020, A&A, 640, A56
Rigault, M., Neill, J. D., Blagorodnova, N., et al. 2019, A&A, 627, A115

Sagiv, I., Gal-Yam, A., Ofek, E. O., et al. 2014, AJ, 147, 79
Sandoval, M. A., Hix, W. R., Messer, O. E. B., Lentz, E. J., & Harris, J. A. 2021, ApJ, 921, 113
Sawada, R., Kashiyama, K., & Suwa, Y. 2022, ApJ, 927, 223
Schlafly, E. F., & Finkbeiner, D. P. 2011, ApJ, 737, 103
Shen, K. J., Kasen, D., Weinberg, N. N., Bildsten, L., & Scannapieco, E. 2010, ApJ, 715, 767
Shingles, L., Smith, K. W., Young, D. R., et al. 2021, TNSAN, 7, 1
Shiode, J. H., & Quataert, E. 2014, ApJ, 780, 96
Shivkumar, H., Jaodand, A. D., Balasubramanian, A., et al. 2023, ApJ, 952, 86
Shvartzvald, Y., Waxman, E., Gal-Yam, A., et al. 2024, ApJ, 964, 74
Smith, K. W., Smartt, S. J., Young, D. R., et al. 2020, PASP, 132, 085002
Sollerman, J. 2002, NewAR, 46, 493
Sollerman, J. 2023, TNSTR, 023-3158, 1
Springob, C. M., Haynes, M. P., Giovanelli, R., & Kent, B. R. 2005, ApJS, 160, 149
Steele, I. A., Smith, R. J., Rees, P. C., et al. 2004, Proc. SPIE, 5489, 679
Stockinger, G., Janka, H. T., Kresse, D., et al. 2020, MNRAS, 496, 2039
Stritzinger, M. D., Taddia, F., Burns, C. R., et al. 2018, A&A, 609, A135
Taddia, F., Sollerman, J., Leloudas, G., et al. 2015, A&A, 574, A60
Taddia, F., Stritzinger, M. D., Bersten, M., et al. 2018, A&A, 609, A136
Tauris, T. M., Langer, N., Moriya, T. J., et al. 2013, ApJL, 778, L23
Tauris, T. M., Langer, N., & Podsiadlowski, P. 2015, MNRAS, 451, 2123
Tonry, J. L., Denneau, L., Heinze, A. N., et al. 2018, PASP, 130, 064505
Turatto, M., Mazzali, P. A., Young, T. R., et al. 1998, ApJL, 498, L129
Valenti, S., Benetti, S., Cappellaro, E., et al. 2008, MNRAS, 383, 1485
Wheeler, J. C., Johnson, V., & Clocchiatti, A. 2015, MNRAS, 450, 1295
Wilkinson, D. M., Maraston, C., Goddard, D., Thomas, D., & Parikh, T. 2017, MNRAS, 472, 4297
Wu, S. C., & Fuller, J. 2022, ApJL, 940, L27
Yan, S., Wang, X., Gao, X., et al. 2023, ApJL, 959, L32
Yao, Y., De, K., Kasliwal, M. M., et al. 2020, ApJ, 900, 46
Yaron, O., & Gal-Yam, A. 2012, PASP, 124, 668
Zhang, W., Woosley, S. E., & Heger, A. 2008, ApJ, 679, 639